

A CLOSE COMPARISON BETWEEN OBSERVED AND MODELED $\text{Ly}\alpha$ LINES FOR $Z \sim 2.2$ LYMAN ALPHA EMITTERS ^{† ‡ ††}

TAKUYA HASHIMOTO ¹, ANNE VERHAMME ², MASAMI OUCHI ^{3,4}, KAZUHIRO SHIMASAKU ^{1,5}, DANIEL SCHAEERER ^{2,6},
KIMIHIKO NAKAJIMA ², TAKATOSHI SHIBUYA ³, MICHAEL RAUCH ⁷, YOSHIAKI ONO ^{3,4}, AND RYOSUKE GOTO ¹.

ABSTRACT

We present the results of a $\text{Ly}\alpha$ profile analysis of 12 $\text{Ly}\alpha$ emitters (LAEs) at $z \sim 2.2$ with high-resolution $\text{Ly}\alpha$ spectra. We find that all 12 objects have a $\text{Ly}\alpha$ profile with the main peak redward of the systemic redshift defined by nebular lines, and five have a weak, secondary peak blueward of the systemic redshift (blue bump). The average velocity offset of the red main peak (the blue bump, if any) with respect to the systemic redshift is $\Delta v_{\text{Ly}\alpha, \text{r}} = 174 \pm 19 \text{ km s}^{-1}$ ($\Delta v_{\text{Ly}\alpha, \text{b}} = -316 \pm 45 \text{ km s}^{-1}$), which is smaller than (comparable to) that of Lyman-break galaxies (LBGs). The outflow velocities inferred from metal absorption lines in three individual and one stacked spectra are comparable to those of LBGs. The uniform expanding shell model constructed by Verhamme et al. (2006) reproduces not only the $\text{Ly}\alpha$ profiles but also other observed quantities including the outflow velocity and the FWHM of nebular lines for the non-blue bump objects. On the other hand, the model predicts too high FWHMs of nebular lines for the blue bump objects, although this discrepancy may disappear if we introduce additional $\text{Ly}\alpha$ photons produced by gravitational cooling. We show that the small $\Delta v_{\text{Ly}\alpha, \text{r}}$ values of our sample can be explained by low neutral-hydrogen column densities of $\log(N_{\text{HI}}) = 18.9 \text{ cm}^{-2}$ on average. This value is more than one order of magnitude lower than those of LBGs but is consistent with recent findings that LAEs have high ionization parameters and low HI gas masses. This result suggests that low N_{HI} values, giving reduced numbers of resonant scattering of $\text{Ly}\alpha$ photons, are the key to the strong $\text{Ly}\alpha$ emission of LAEs.

Subject headings: galaxies: high-redshift — galaxies: ISM — line: profiles — radiative transfer

1. INTRODUCTION

$\text{Ly}\alpha$ emitters (LAEs) are objects commonly seen in both the local and high- z universes with large $\text{Ly}\alpha$ equivalent widths, $\text{EW}(\text{Ly}\alpha) \gtrsim 20 - 30 \text{ \AA}$ (local: Deharveng et al. 2008; Cowie et al. 2011, high- z : Hu & McMahon 1996; Rhoads & Malhotra 2001; Ouchi et al. 2008, 2010). Previous studies based on Spectral Energy Distributions (SEDs) have revealed that typical LAEs are young, low-mass galaxies with a small dust content (e.g., Nilsson et al. 2007; Gawiser et al. 2007; Guaita et al. 2011; Nakajima et al.

2012; Kusakabe et al. 2015), although there are some evolved LAEs with a moderate mass and dust (Ono et al. 2010b; Hagen et al. 2014). Morphological studies of their UV continuum have shown that the galactic counterparts of LAEs to be typically compact (e.g., Bond et al. 2009) and their typical size does not evolve with redshift (Malhotra et al. 2012). Furthermore, clustering analyses have revealed that LAEs have the lowest dark matter halo masses at every redshift (Ouchi et al. 2010; Guaita et al. 2010). These properties suggest that LAE is an important galaxy population as the building block candidates in the Λ CDM model (Rauch et al. 2008).

Given their importance in galaxy evolution, the $\text{Ly}\alpha$ escape mechanism in LAEs is still poorly understood. Resonant scattering strongly extends the path-length of $\text{Ly}\alpha$ photons through galactic gas and renders them prone to absorption by dust grains. On one hand, some observational studies at the local universe have proposed that outflows facilitate the escape of $\text{Ly}\alpha$ photons from galaxies (e.g., Kunth et al. 1998) as they reduce the number of scattering. Likewise, others (e.g., Kornei et al. 2010; Atek et al. 2014) have shown that the dust content correlates with $\text{Ly}\alpha$ emissivity. While these effects would certainly be at work, there has been no decisive conclusion (cf., Cassata et al. 2015). On the other hand, theoretical studies have computed the $\text{Ly}\alpha$ radiation transfer (RT) through idealized spherically symmetric shells of homogeneous and isothermal neutral hydrogen gas, especially in a form of an expanding shell (e.g., Zheng & Miralda-Escudé 2002; Verhamme et al. 2006; Dijkstra & Loeb 2009; Kollmeier et al. 2010). They have investigated how properties of the interstellar medium

thashimoto_at_astron.s.u-tokyo.ac.jp

¹ Department of Astronomy, Graduate School of Science, The University of Tokyo, Tokyo 113-0033, Japan

² Observatoire de Genève, Université de Genève, 51 Ch. des Maillettes, 1290 Versoix, Switzerland

³ Institute for Cosmic Ray Research, The University of Tokyo, 5-1-5 Kashiwanoha, Kashiwa, Chiba 277-8582, Japan

⁴ Kavli Institute for the Physics and Mathematics of the Universe (WPI), The University of Tokyo, 5-1-5 Kashiwanoha, Kashiwa, Chiba 277-8583, Japan

⁵ Research Center for the Early Universe, Graduate School of Science, The University of Tokyo, Tokyo 113-0033, Japan

⁶ CNRS, IRAP, 14 Avenue E. Belin, 31400 Toulouse, France

⁷ Observatories of the Carnegie Institution of Washington, 813 Santa Barbara Street, Pasadena, CA 91101, USA

[†] Some of the data presented herein were obtained at the W. M. Keck Observatory, which is operated as a scientific partnership among the California Institute of Technology, the University of California, and the National Aeronautics and Space Administration. The Observatory was made possible by the generous financial support of the W. M. Keck Foundation.

[‡] Based in part on data collected at the Subaru Telescope, which is operated by the National Astronomical Observatory of Japan.

^{††} This paper includes data gathered with the 6.5 meter Magellan Telescopes located at Las Campanas Observatory, Chile.

(ISM) affect the Ly α escape and emergent Ly α profiles. The result is that the Ly α RT is a complicated process altered by galactic outflows/inflows, the neutral hydrogen column density and dust content of the ISM, and the inclination of the galaxy disk (e.g., Verhamme et al. 2012; Zheng & Wallace 2014; Behrens & Braun 2014). One of the goals in these theoretical studies is to aid understanding the galaxy properties from observed Ly α lines, and to identify the key factor for the Ly α escape.

To study the Ly α RT and escape through close comparisons of observed and modeled Ly α lines, it is important to obtain spectral lines other than the Ly α line. The central wavelength and the width of nebular lines (e.g., H α and [OIII]) tell us the galaxy's systemic redshift and internal velocity. The blue-shift of interstellar (IS) absorption lines with respect to the systemic redshift gives the galactic outflow velocity, and the width of the IS lines can be interpreted as the sum of thermal and macroscopic (rotation and turbulence) velocities of the outflowing gas. These lines can help us to disentangle the complicated Ly α RT and understand the Ly α escape.

However, due to the typical faintness of LAEs, it is only recently that these additional lines have been successfully detected in narrow-band selected LAEs (nebular lines: e.g., McLinden et al. 2011; Finkelstein et al. 2011; Hashimoto et al. 2013, IS absorption lines: Hashimoto et al. 2013; Shibuya et al. 2014b). Thus, in contrast to LBGs whose Ly α profiles have been closely compared with Ly α RT models (e.g., Verhamme et al. 2008; Kulas et al. 2012; Christensen et al. 2012), there are only a few studies that have performed Ly α profile comparisons of LAEs (e.g., Chonis et al. 2013). Recent simultaneous detections of Ly α and nebular emission lines have statistically confirmed that the Ly α profiles of LAEs are asymmetric with a red main peak redshifted with respect to the systemic $\Delta v_{\text{Ly}\alpha, \text{r}} > 0 \text{ km s}^{-1}$ (e.g., Shibuya et al. 2014b; Song et al. 2014; Erb et al. 2014). Likewise, IS absorption studies in LAEs have shown that they are blue-shifted with respect to the systemic by $|\Delta v_{\text{abs}}| \sim 100 - 200 \text{ km s}^{-1}$ (Hashimoto et al. 2013; Shibuya et al. 2014b), which is comparable to those of LBGs (e.g., Pettini et al. 2001; Shapley et al. 2003; Steidel et al. 2010; Kulas et al. 2012). These results suggest that LAEs do have outflows and motivate us to apply expanding shell models to LAEs.

To examine Ly α escape mechanisms in LAEs through detailed Ly α modeling, we focus on the small $\Delta v_{\text{Ly}\alpha, \text{r}}$ of LAEs, $\Delta v_{\text{Ly}\alpha, \text{r}} \simeq 200 \text{ km s}^{-1}$, compared to those of LBGs, $\Delta v_{\text{Ly}\alpha, \text{r}} \simeq 400 \text{ km s}^{-1}$ (e.g., Steidel et al. 2010; Kulas et al. 2012), with similar physical quantities such as stellar mass, star formation rate (SFR), and velocity dispersion (Hashimoto et al. 2013; Shibuya et al. 2014b; Song et al. 2014; Erb et al. 2014). Hashimoto et al. (2013) and Shibuya et al. (2014b) have also shown that LAEs have comparable outflow velocities, measured from IS absorption lines, to those of LBGs. These results imply that a definitive difference between LAEs and LBGs in velocity properties is $\Delta v_{\text{Ly}\alpha, \text{r}}$. In addition, Hashimoto et al. (2013) have demonstrated that EW(Ly α) anti-correlates with $\Delta v_{\text{Ly}\alpha, \text{r}}$ using a large sample of LAEs and LBGs (see also Shibuya et al. 2014b; Erb et al. 2014). Therefore, understanding the reason why LAEs have small $\Delta v_{\text{Ly}\alpha, \text{r}}$, through detailed Ly α

modeling should shed light on the Ly α RT and Ly α escape mechanisms in LAEs.

According to the theoretical studies, there are several possible explanations for a small $\Delta v_{\text{Ly}\alpha, \text{r}}$: a high outflow velocity (e.g., Verhamme et al. 2006), a very low neutral hydrogen column density (N_{HI}) of the ISM (e.g., Verhamme et al. 2006, 2015), an inhomogeneous ISM with a covering fraction (CF) below unity, where CF is defined as the fraction of sightlines which are optically thick to the Ly α radiation, i.e., gas with holes (e.g., Behrens et al. 2014; Verhamme et al. 2015), and a clumpy ISM with a low covering factor, f_c , which is defined as the average number of clouds intersected by a random line of sight (e.g., Hansen & Oh 2006; Dijkstra & Kramer 2012; Laursen et al. 2013).

In this work, we focus on applying the uniform expanding shell model based on a 3D Ly α RT constructed by Verhamme et al. (2006) and Schaerer et al. (2011), to 12 LAEs whose Ly α and nebular emission lines (e.g., H α , OIII) have been observed at a high spectral resolution (Hashimoto et al. 2013; Nakajima et al. 2013; Shibuya et al. 2014b). With the systemic redshifts and the full width half maximums (FWHM) determined from nebular emission lines, the stellar dust extinction derived from SED fitting, and the galactic outflow velocities inferred from LIS absorption lines, we first statistically examine how well the model can reproduce the Ly α profiles and other observables (cf., Verhamme et al. 2008; Kulas et al. 2012; Chonis et al. 2013). After demonstrating the validity of the model, we securely derive physical quantities such as N_{HI} and discuss the origin of the small $\Delta v_{\text{Ly}\alpha, \text{r}}$ and implications for the Ly α escape in LAEs. Possible other scenarios mentioned above for the small $\Delta v_{\text{Ly}\alpha, \text{r}}$ are also qualitatively discussed.

This paper is organized as follows. We describe our spectroscopy observations in Section 2, and discuss profiles of Ly α and nebular emission lines in Section 3. We apply the uniform expanding shell model to our data and show comparisons with observables in Section 4. Discussion on the blue bumps as well as the origin of the small Ly α velocity offsets are given in Section 5, followed by conclusions in Section 6.

Throughout this paper, magnitudes are given in the AB system (Oke & Gunn 1983), and we assume a Λ CDM cosmology with $\Omega_m = 0.3$, $\Omega_\Lambda = 0.7$ and $H_0 = 70 \text{ km s}^{-1} \text{ Mpc}^{-1}$.

2. DATA AND OBSERVATIONS

Our initial sample of objects are taken from large $z \sim 2.2$ LAE samples in the COSMOS field, the Chandra Deep Field South (CDFS), and the Subaru/XMM-Newton Deep Survey (SXDS) (Nakajima et al. 2012, 2013; Nakajima et al. in prep.). These LAE samples are all based on Subaru/Suprime-Cam imaging observations with our custom made narrow band filter, NB387 ($\lambda_c = 3870 \text{ \AA}$ and FWHM = 94 \AA). The LAEs have been selected by color criteria of $B - \text{NB387}$ and $u^* - \text{NB387}$, satisfying the condition that the rest frame photometric Ly α EW (EW(Ly α)_{photo}) be larger than 30 \AA . From these, we only use 12 LAEs whose Ly α and nebular emission lines (e.g., H α and [OIII]) are both spectroscopically confirmed. Among the 12 objects, 11 have been presented in Hashimoto et al. (2013) and Shibuya et al. (2014b). We

add one new LAE with $\text{EW}(\text{Ly}\alpha)_{\text{photo}} \sim 280\text{\AA}$ whose detailed properties will be discussed in Hashimoto et al. in prep.

In this section, we briefly summarize our near-infrared spectroscopy (§2.1), optical spectroscopy (§2.2), and the contamination of AGNs in the sample (§2.3).

2.1. Near-Infrared Spectroscopy

In order to detect nebular emission lines, we performed three near-infrared observations with Magellan/MMIRS (PI: M. Ouchi), Keck/NIRSPEC (PI: K. Nakajima), and Subaru/FMOS (PI: K. Nakajima). Canonical spectral resolutions for our observation settings are $R \sim 1120$, 1500, and 2200 for MMIRS, NIRSPEC, and FMOS, respectively.

Details of the observation and data reduction procedures for MMIRS and NIRSPEC have been presented in Hashimoto et al. (2013) and Nakajima et al. (2013), respectively. Briefly, two CDFS objects, CDFS-3865 and CDFS-6482, were observed with MMIRS using the HK grism covering $2.254 - 2.45\ \mu\text{m}$, resulting in successful H α and [OIII] $\lambda\lambda$ 4959 5007 detections. A follow-up observation was carried out for CDFS-3865 with NIRSPEC. The [OII] λ 3727 line was additionally detected with the J band ($1.15 - 1.36\ \mu\text{m}$). Four COSMOS objects, COSMOS-08501, COSMOS-13636, COSMOS-30679, and COSMOS-43982, were observed with NIRSPEC and its K band ($2.2 - 2.43\ \mu\text{m}$), resulting in H α line detections. The [OIII] λ 5007 line was also detected from COSMOS-30679 using the H band ($1.48 - 1.76\ \mu\text{m}$).

The data from FMOS will be presented in Nakajima et al. (2015, in prep). Its spectral coverage is $0.9 - 1.8\ \mu\text{m}$. We detected [OIII] line(s) in eight objects: COSMOS-08357, COSMOS-12805, COSMOS-13138, COSMOS-13636, COSMOS-38380, COSMOS-43982, SXDS-10600, and SXDS-10942.

2.2. Optical Spectroscopy

In order to detect Ly α and metal absorption lines, we carried out several observations with Magellan/MagE (PI: M. Rauch) and Keck/LRIS (PI: M. Ouchi). The spectral resolutions for our observations were $R \sim 4100$ and ~ 1100 for MagE and LRIS, respectively. The slit was positioned on the Ly α centroids in the NB387 images.

Details of the observation and data reduction procedures for MagE and LRIS have been presented in Hashimoto et al. (2013) and Shibuya et al. (2014b), respectively, except for COSMOS-08501. First, we describe this new object in detail (§2.2.1) and then give a brief summary for the rest of the sample (§2.2.2).

2.2.1. Optical Spectroscopy for COSMOS-08501

The MagE observations were carried out for COSMOS-08501 on 2012 February and 2013 December. We obtained $3 \times 3000\text{ s}$ and $1 \times 3000\text{ s}$ exposure times during each run, resulting in a 12000 s total integration time. Spectroscopic standard stars, dome flats, and Xenon flash lamp flats, were obtained on each night for calibrations. On these nights, the typical seeing sizes were $1''.0$. The slit width was $1''.0$ for both runs, corresponding to $R \sim 4100$. The spectra were reduced with IDL based pipeline, **MagE-REDUCE**, constructed by G. Becker (see

also Kelson 2003). This pipeline processes raw frames, performing wavelength calibration and optimal sky subtraction, and extracts 1D spectra. Each of these reduced frames was then combined to form our final calibrated spectrum. From this, the Ly α line was identified above the $3\ \sigma$ noise of the local continuum.

2.2.2. Optical Spectroscopy for the Rest of the Sample

CDFS-3865, CDFS-6482, and COSMOS-30679 were observed with MagE; COSMOS-08357, COSMOS-12085, COSMOS-13138, COSMOS-38380, SXDS-10600, and SXDS-10942 were observed with LRIS; and finally, COSMOS-13636 and COSMOS-43982 were observed with both spectrographs. We identified the Ly α line in all objects. In addition, we detected several metal absorption lines (e.g., Si II λ 1260 and C IV λ 1548 lines) in a stacked MagE spectrum of CDFS-3865, CDFS-6482, COSMOS-13636, and COSMOS-30679 (Hashimoto et al. 2013) as well as in individual LRIS spectra of COSMOS-12805, COSMOS-13636, and SXDS-10600 (Shibuya et al. 2014b).

A summary of our observations is listed in Table 1, and our Ly α and nebular emission line profiles are shown in Figure 1.

2.3. AGNs in the Sample

The presence of AGNs in the MagE objects has been examined in Hashimoto et al. (2013) and Nakajima et al. (2013), and those of the LRIS objects in Shibuya et al. (2014b).

In short, for the MagE objects, we inspected it in three ways. We first compared the sky coordinates of the objects with those in very deep archival X-ray and radio catalogs. Then we checked for the presence of high ionization state lines such as C IV λ 1549 and He II λ 1640 lines in the spectra. Finally, we applied the BPT diagnostic diagram (Baldwin et al. 1981) to the objects. No AGN activity is seen except for COSMOS-43982 whose high [NII] /H α line ratio is consistent with that of an AGN.

On the other hand, due to the lack of H α or [NII] λ 6568 data, we were only able to use the two forms of investigation for the LRIS objects. Of these, only COSMOS-43982 showed clear detection of the C IV λ 1549 line in its optical spectrum.

In summary, we have ruled out AGN activity in all but COSMOS-43982.

3. OBSERVATIONAL RESULTS

3.1. Line Center and FWHM Measurements for Nebular Emission Lines

Line center (i.e., redshift) and FWHM measurements of nebular emission lines are crucial for a detailed modeling of the Ly α line, since they encode information on the intrinsic (i.e., before being affected by radiative transfer) Ly α redshift and FWHM. In order to obtain these parameters and their uncertainties, we apply a Monte Carlo technique as follows. First, for each line of each object, we measure the 1σ noise of the local continuum. Then we create 10^3 fake spectra by perturbing the flux at each wavelength of the true spectrum by the measured 1σ error (Kulas et al. 2012; Chonis et al. 2013). For each fake spectrum, the wavelength at the highest flux peak

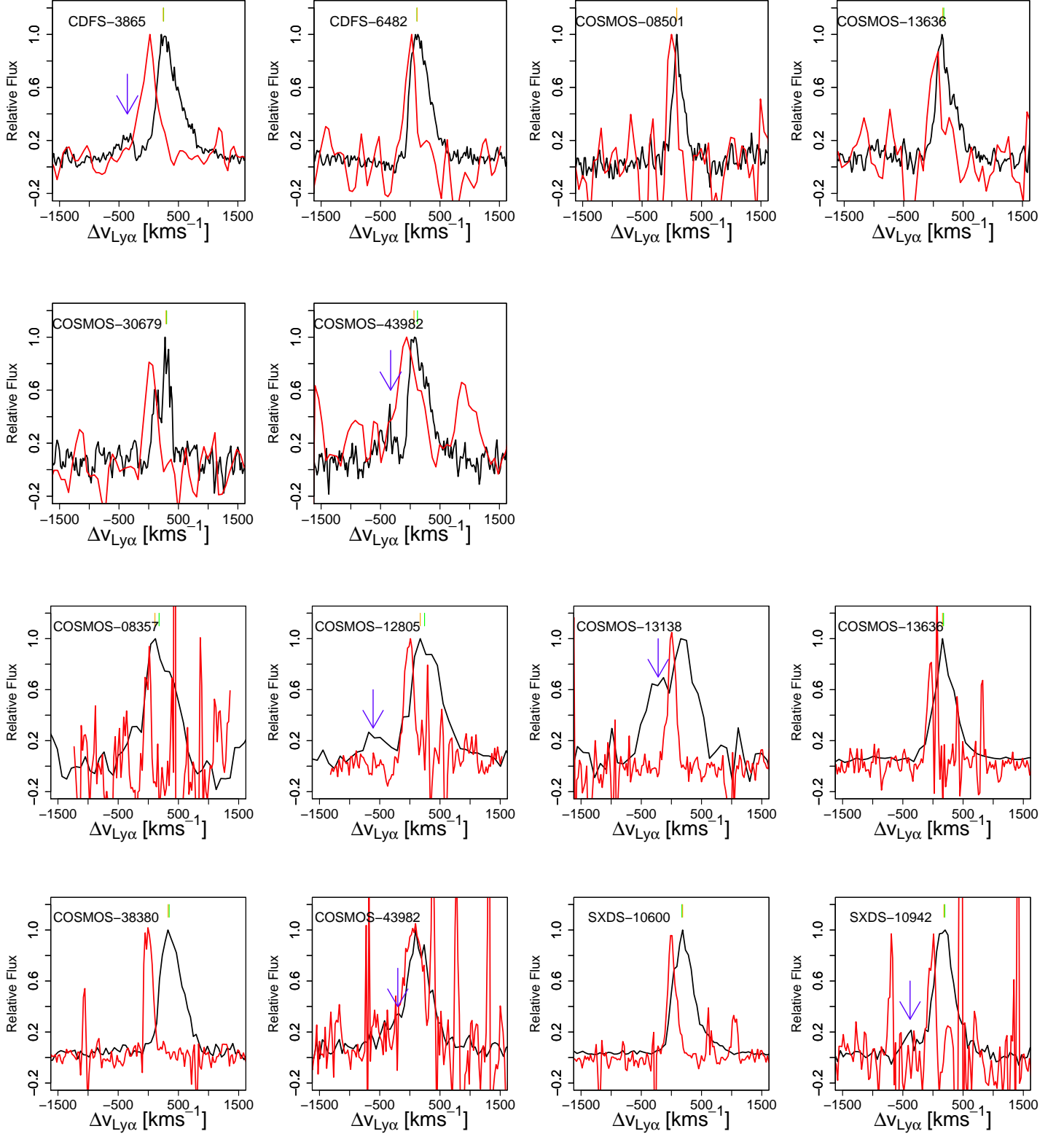


FIG. 1.— The upper two rows of panels show the Ly α lines (black) obtained with MagE and the corresponding H α lines (red), while the lower two rows of panels show the Ly α lines obtained with LRIS (black) and the [OIII] lines (red). Blue arrows denote blue bumps. All spectra are scaled to the wavelength range from -1500 to $+1500$ km s $^{-1}$. Yellow and green segments indicate the peak flux positions derived from a symmetric Gaussian and a Monte Carlo technique, respectively.

TABLE 1
SUMMARY OF THE OBSERVATIONS

Object	α (J2000)	δ (J2000)	EW(Ly α) _{photo} (\AA) (4)	$L(\text{Ly}\alpha)$ ($10^{42} \text{ erg s}^{-1}$) (5)	NIR obs.	opt. obs.	Source ^a
(1)	(2)	(3)	(4)	(5)	(6)	(7)	(8)
CDFS-3865	03:32:32.31	-28:00:52.20	64 ± 29	29.8 ± 4.9	NIRSPEC (J) MMIRS (HK)	MagE	H13, N13
CDFS-6482	03:32:49.34	-27:59:52.35	76 ± 52	15.4 ± 8.1	MMIRS (HK)	MagE	H13, N13
COSMOS-08501	10:01:16.80	+02:05:36.26	280 ± 30	8.8 ± 1.1	NIRSPEC (K)	MagE	N13
COSMOS-30679	10:00:29.81	+02:18:49.00	87 ± 7	8.5 ± 0.7	NIRSPEC (H and K)	MagE	H13, N13
COSMOS-13636	09:59:59.38	+02:08:38.36	73 ± 5	11.3 ± 0.5	FMOS (H) NIRSPEC (K)	MagE and LRIS	H13, N13, S14
COSMOS-43982 ^b	09:59:54.39	+02:26:29.96	130 ± 12	11.0 ± 0.5	MMIRS (HK)	MagE and LRIS	H13, N13, S14
COSMOS-08357	09:59:59.07	+02:05:31.60	47 ± 8	0.5 ± 0.1	FMOS (H)	LRIS	S14, N15
COSMOS-12805	10:00:15.29	+02:08:07.50	34 ± 6	2.6 ± 0.3	FMOS (H)	LRIS	S14, N15
COSMOS-13138	10:00:02.61	+02:08:24.50	40 ± 10	0.4 ± 0.1	FMOS (H)	LRIS	S14, N15
COSMOS-38380	09:59:40.94	+02:23:04.20	137 ± 15	2.6 ± 0.3	FMOS (H)	LRIS	S14, N15
SXDS-10600	02:17:46.09	-06:57:05.00	58 ± 3	1.9 ± 0.1	FMOS (H)	LRIS	S14, N15
SXDS-10942	02:17:59.54	-06:57:25.60	135 ± 10	0.3 ± 0.0	FMOS (H)	LRIS	S14, N15

NOTE. — (1) Object ID; (2), (3) Right Ascension and Declination; (4), (5) rest-frame Ly α EW and luminosity derived from narrow- and broadband photometry; (6) Instruments and filters used for the NIR observations; (7) Instruments used for the optical observations; and (8) Source of the information

^a H13: Hashimoto et al. (2013); N13: Nakajima et al. (2013); S14: Shibuya et al. (2014b); N15: Nakajima et al (2015, in preparation)

^b AGN-like object

is adopted as the line center, and the wavelength range encompassing half the maximum flux is adopted as the FWHM. The standard deviation of the distribution of measurements from the 10^3 artificial spectra is adopted as the error on the line center and FWHM. When multiple lines are detected, we adopt a weighted mean value of them. A summary of the measurements are listed in the columns 2 and 3 of Table 2. All redshift (FWHM) values are corrected for the LSR motion (instrumental resolution). When the line is unresolved, the instrumental resolution is given as an upper limit. The mean FWHM value for a sample of eight objects with a measurable velocity dispersion is $\text{FWHM}(\text{neb}) = 129 \pm 55 \text{ km s}^{-1}$, which is smaller than that of LBGs, $\text{FWHM}(\text{neb}) = 200 - 250 \text{ km s}^{-1}$ (Pettini et al. 2001; Erb et al. 2006a; Kulas et al. 2012). This is consistent with the recent results by Erb et al. (2014), who have found that the median $\text{FWHM}(\text{neb})$ of $36 \lesssim z \lesssim 2$ LAEs is 127 km s^{-1} . These results indicate that LAEs have smaller dynamical masses than LBGs.

3.2. Two Component [OIII] Profiles

Among the nebular emission lines we have obtained, while most objects show normal symmetric Gaussian profiles, COSMOS-13138 and SXDS-10600 show an asymmetric [OIII] profile with a secondary blueshifted and redshifted component, respectively (see Figure 2). Such a profile has been reported in various objects: both local and high- z star-forming galaxies and ULIRGs (e.g., Shapiro et al. 2009; Genzel et al. 2011; Newman et al. 2012; Soto et al. 2012), a high- z Oxygen-Two Blob ([OII] blob) (Harikane et al. 2014), and a few Lyman-Alpha Blobs (LABs) (Yang et al. 2014). However in LAEs, there has been no study which reports its presence.

Aforementioned studies apply a two Gaussian components fit with a narrow and broad components to the line. To examine the presence of two components, we also perform a fit with two Gaussians. We have six parameters: fluxes, line centers, and FWHMs for both components. We require that the widths of both components are larger than the spectral resolution, and that the broad component has a larger FWHM than the narrow component. Best fit parameters are determined through minimum χ^2 realizations, and the parameter range satisfying $\chi^2 \leq \chi_{\min}^2 + 1$ is adopted as the error, where χ_{\min}^2 denotes the minimum χ^2 value. The results are listed in Table 3. For each object, both components are significantly detected with $\gtrsim 4\sigma$, demonstrating that some fraction of LAEs have two-component line profiles.

The velocity offsets of the two components are $104 \pm 11 \text{ km s}^{-1}$ (COSMOS-13138) and $115 \pm 8 \text{ km s}^{-1}$ (SXDS-10600), respectively.

The FWHM values of the broad component after correction for instrumental resolution are 70 ± 50 and $80 \pm 30 \text{ km s}^{-1}$. These are much smaller than those of the star-forming galaxies at $z \sim 2$ ($\text{FWHM} = 300 - 1000 \text{ km s}^{-1}$, Genzel et al. 2011), and slightly smaller than those of the [OII] blob ($\text{FWHM} = 120 - 130 \text{ km s}^{-1}$) of Harikane et al. (2014) and the LABs ($\text{FWHM} = 100 - 280 \text{ km s}^{-1}$) of Yang et al. (2014). Our small values exclude the possibility of the broad component originating from an AGN activity (cf., Osterbrock & Ferland 2006) or a powerful outflow driven by a starburst (e.g., Shapiro et al. 2009;

Genzel et al. 2011; Newman et al. 2012) because in these cases, the FWHM of the broad component should be as large as $\sim 300 - 1000 \text{ km s}^{-1}$. It is possible that the two component lines originate from two large star-forming regions (e.g., Harikane et al. 2014) or mergers. As discussed in Harikane et al. (2014), the velocity offset of the two components, $\sim 100 \text{ km s}^{-1}$, may be due to a rotation of the objects.

3.3. Ly α Profile with a Blue Bump

While the majority of Ly α profiles are single-peaked (e.g., Shapley et al. 2003; Steidel et al. 2010), a fraction of Ly α profiles are known to be multiple-peaked (e.g., Rauch et al. 2008; Yamada et al. 2012; Kulas et al. 2012). In particular, we shall refer to a secondary small peak blueward of the systemic redshift as “the bluebump” (see the case 2 profile in Figure 12 in Verhamme et al. 2006). Theoretical studies have shown that the blue bump is a natural outcome of the radiative transfer in a low speed galactic outflow (e.g., Zheng & Miralda-Escudé 2002).

We consider a blue bump to be detected if there exists an excess emission blueward of the systemic redshift above 3σ noise of the local continuum. We detect a blue bump of five objects; the MagE ones of CDFS-3865 and COSMOS-43982, and the LRIS ones of COSMOS-12805, COSMOS-13138, COSMOS-43982, and SXDS-10942 (the column 4 of Table 2). The position of the blue bump is designated by a blue arrow in Figure 1.

The frequency of blue-bump objects in the sample is $\sim 40\%$ (5/12). There are four LAEs in the literature that have a blue bump: one among the two LAEs studied in McLinden et al. (2011) and all three LAEs studied in Chonis et al. (2013). For the total sample of 17 LAEs, the frequency is calculated to be $\sim 50\%$ (9/17). Note that this is a lower limit due to the limited spectral resolution. On the other hand, Kulas et al. (2012) have studied 18 $z \sim 2 - 3$ LBGs with z_{sys} measurements which are preselected to have multiple-peaked Ly α profiles. They have argued that $\sim 30\%$ of the parent sample are multiple-peaked and that 11 out of the 18 objects have a blue bump, indicating that the blue bump frequency in LBGs is $\sim 20\%$ ($\sim 30\% \times 11/18$). These results imply that the blue bump feature is slightly more common in LAEs than in LBGs although a larger sample observed at higher spectral resolution is needed for a definite conclusion.

3.4. Ly α Velocity Properties

We derive three velocity offsets related to the Ly α line: the velocity offset of the main red peak of the Ly α line with respect to the systemic redshift,

$$\Delta v_{\text{Ly}\alpha, \text{r}} = c \frac{z_{\text{Ly}\alpha, \text{r}} - z_{\text{sys}}}{1 + z_{\text{sys}}}, \quad (1)$$

that of the blue bump of the Ly α line with respect to the systemic redshift, if any,

$$\Delta v_{\text{Ly}\alpha, \text{b}} = c \frac{z_{\text{Ly}\alpha, \text{b}} - z_{\text{sys}}}{1 + z_{\text{sys}}}, \quad (2)$$

and that of the two peaks,

$$\Delta v_{\text{peak}} = \Delta v_{\text{Ly}\alpha, \text{r}} - \Delta v_{\text{Ly}\alpha, \text{b}}, \quad (3)$$

TABLE 2
SUMMARY OF THE OBSERVED SPECTROSCOPIC PROPERTIES OF THE SAMPLE

Object	z_{sys}	FWHM(neb) (km s ⁻¹)	Blue Bump	$\Delta v_{\text{Ly}\alpha, \text{r}}$ (km s ⁻¹)	$\Delta v_{\text{Ly}\alpha, \text{b}}$ (km s ⁻¹)	Δv_{peak} (km s ⁻¹)	EW(Ly α) _{spec} (Å)	S_w
(1)	(2)	(3)	(4)	(5)	(6)	(7)	(8)	(9)
CDFS-3865	2.17242 ± 0.00016	242 ± 31	yes	245 ± 36	-352 ± 59	597 ± 67	40 ± 2	8.8 ± 0.3
CDFS-6482	2.20490 ± 0.00042	99^{+66}_{-99}	no	118 ± 48	-	-	26 ± 2	6.6 ± 1.7
COSMOS-08501	2.16161 ± 0.00042	< 200	no	82 ± 40	-	-	10 ± 1	2.2 ± 2.7
COSMOS-30679	2.19725 ± 0.00020	92 ± 45	no	290 ± 33	-	-	10 ± 1	3.1 ± 1.0
COSMOS-13636 (MagE)	2.16075 ± 0.00019	73 ± 5	no	146 ± 25	-	-	23 ± 5	5.3 ± 1.0
COSMOS-13636 (LRIS)	2.16075 ± 0.00019	73 ± 5	no	161 ± 18	-	-	26 ± 1	6.2 ± 0.5
COSMOS-43982 (MagE)	2.19267 ± 0.00036	325 ± 36	yes	117 ± 53	-297 ± 57	414 ± 78	24 ± 17	7.9 ± 1.3
COSMOS-43982 (LRIS)	2.19267 ± 0.00036	325 ± 36	yes	155 ± 40	-165 ± 90	320 ± 98	42 ± 3	-4.2 ± 0.6
COSMOS-08357	2.18053 ± 0.00031	< 136	no	106 ± 71	-	-	19 ± 3	-4.2 ± 7.9
COSMOS-12805	2.15887 ± 0.00024	110 ± 16	yes	171 ± 25	-605 ± 114	776 ± 117	24 ± 1	8.9 ± 0.7
COSMOS-13138	2.17914 ± 0.00012	63 ± 6	yes	191 ± 59	-214 ± 87	405 ± 105	46 ± 11	-1.6 ± 4.8
COSMOS-38380	2.21245 ± 0.00015	99 ± 9	no	338 ± 21	-	-	73 ± 7	2.5 ± 0.8
SXDS-10600	2.20922 ± 0.00014	55 ± 28	no	186 ± 13	-	-	44 ± 1	11.7 ± 0.2
SXDS-10942	2.19574 ± 0.00025	< 136	yes	135 ± 10	-374 ± 41	556 ± 66	94 ± 10	1.3 ± 0.3

NOTE. — The symbol “-” indicates we have no measurement. (1) Object ID; (2) Systemic redshift derived from the weighted mean of the nebular emission redshifts; (3) Weighted mean FWHM of nebular emission line; (4) Presence of a blue bump emission in the Ly α profile; (5) Velocity offset of the Ly α main red peak with respect to z_{sys} ; (6) Velocity offset of the Ly α blue-bump with respect to z_{sys} ; (7) Separation between $\Delta v_{\text{Ly}\alpha, \text{r}}$ and $\Delta v_{\text{Ly}\alpha, \text{b}}$; (8) Rest-frame Ly α EW derived from spectroscopy; and (9) Weighted skewness of the Ly α line.

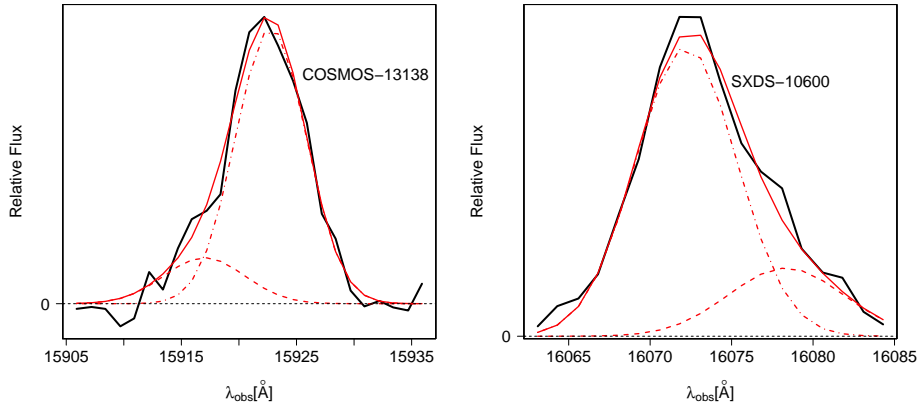


FIG. 2.— [OIII] $\lambda 5007$ spectrum of COSMOS-13138 (left panel) and SXDS-10600 (right) taken by FMOS. The black solid lines are the observed spectra. There is a broad component in addition to a narrow component. The red solid lines denote the best-fit functions for the whole lines, and the red dashed lines represent those of the individual components.

where z_{sys} , $z_{\text{Ly}\alpha, \text{r}}$, and $z_{\text{Ly}\alpha, \text{b}}$ represent the systemic redshift, the Ly α redshift of the main red peak, and that of the blue bump, respectively.

3.4.1. Ly α Main Red Peak Velocity Offsets, $\Delta v_{\text{Ly}\alpha, \text{r}}$

We estimate the $\Delta v_{\text{Ly}\alpha, \text{r}}$ value using a Monte Carlo technique in a similar manner to that in §3.1. First, for each object, we measure the 1σ error in the Ly α spectrum set by the continuum level at the wavelength longer than 1216\AA . Then we create 10^3 fake spectra converted to velocity space by simultaneously perturbing the flux

at each wavelength and the systemic redshift listed in Table 2 by their 1σ errors. Finally, we measure the velocity at the highest flux peak. The mean and the standard deviation value of the distribution of 10^3 measurements are adopted as the $\Delta v_{\text{Ly}\alpha, \text{r}}$ and its error, respectively. The derived $\Delta v_{\text{Ly}\alpha, \text{r}}$ values are listed in the column 5 of Table 2, ranging from 82 km s^{-1} to 338 km s^{-1} with a mean value of $174 \pm 19 \text{ km s}^{-1}$. In most cases, these values are consistent with those measured in Hashimoto et al. (2013) and Shibuya et al. (2014b) within 1σ , however, they are not for COSMOS-08357 and COSMOS-12805.

TABLE 3
SUMMARY OF THE TWO-COMPONENT FITS FOR [OIII] LINE

Object (1)	f_{narrow} (10^{-17} erg s $^{-1}$ cm $^{-2}$) (2)	f_{broad} (10^{-17} erg s $^{-1}$ cm $^{-2}$) (3)	z_{narrow} (4)	z_{broad} (5)	FWHM $_{\text{narrow}}$ (km s $^{-1}$) (6)	FWHM $_{\text{broad}}$ (km s $^{-1}$) (7)
COSMOS-13138	4.7 ± 0.2	0.9 ± 0.2	2.17931 ± 0.00002	2.17821 ± 0.00012	30 ± 20	70 ± 50
SXDS-10600	14.9 ± 0.6	4.2 ± 0.6	2.20915 ± 0.00002	2.21038 ± 0.00008	20 ± 30	80 ± 30

NOTE. — (1) Object ID; (2), (3) Fluxes of the narrow (f_{narrow}) and the broad (f_{broad}) components. Note that the values are not corrected for the slit loss; (4), (5) Redshifts of the narrow (z_{narrow}) and the broad (z_{broad}) components; (6), (7) FWHM measurements of the narrow (FWHM $_{\text{narrow}}$) and the broad (FWHM $_{\text{broad}}$) components.

This is due to the fact that these studies have applied a symmetric/asymmetric profile fit to the Ly α line. In Figure 1, we show the two $\Delta v_{\text{Ly}\alpha, \text{r}}$ values derived from the Monte Carlo and the profile fit technique as the orange and green line segments, respectively. For the sake of consistency in the definition of the $\Delta v_{\text{Ly}\alpha, \text{r}}$ in the shell model (Verhamme et al. 2006; Schaerer et al. 2011), we adopt here the new measurements. We note that our discussion is unchanged even if we adopt the previous $\Delta v_{\text{Ly}\alpha, \text{r}}$ values.

The $\Delta v_{\text{Ly}\alpha, \text{r}}$ value has been measured in more than 60 LAEs (McLinden et al. 2011; Finkelstein et al. 2011; Hashimoto et al. 2013; Guaita et al. 2013; Chonis et al. 2013; Shibuya et al. 2014b; Song et al. 2014; Erb et al. 2014). These studies have shown that LAEs at $z \sim 2-3$ have a mean $\Delta v_{\text{Ly}\alpha, \text{r}}$ of $\simeq 200$ km s $^{-1}$, which is significantly smaller than that of LBGs at a similar redshift, $\Delta v_{\text{Ly}\alpha, \text{r}} \simeq 400$ km s $^{-1}$ (e.g., Steidel et al. 2010; Rakic et al. 2011; Kulas et al. 2012). The left panel of Figure 3 represents the histogram of $\Delta v_{\text{Ly}\alpha, \text{r}}$ for the 12 LAEs (14 spectra) studied in this study and 18 LBGs given by Kulas et al. (2012). We carry out the Kolmogorov-Smirnov (K-S) test for the two populations. The resultant probability is 10^{-6} , indicating that $\Delta v_{\text{Ly}\alpha, \text{r}}$ is definitively different between LAEs and LBGs.

3.4.2. Ly α Blue Bump Velocity Offsets, $\Delta v_{\text{Ly}\alpha, \text{b}}$

For each detected blue bump in §3.3, we measure $\Delta v_{\text{Ly}\alpha, \text{b}}$ value in the same manner as for $\Delta v_{\text{Ly}\alpha, \text{r}}$. We obtain $\Delta v_{\text{Ly}\alpha, \text{b}} = -352 \pm 59$ km s $^{-1}$ (CDFS-3865), -297 ± 57 km s $^{-1}$ (MagE-COSMOS-43982), -605 ± 114 km s $^{-1}$ (COSMOS-12805), -214 ± 87 km s $^{-1}$ (COSMOS-13138), -165 ± 90 km s $^{-1}$ (LRIS-COSMOS-43982), and -374 ± 41 km s $^{-1}$ (SXDS-10942) as listed in the column 6 of Table 2. We have obtained two different measurements for COSMOS-43982 due to the spectral resolution effect, however, they are consistent with each other within 1σ (see also §4.3.3). We combine our $\Delta v_{\text{Ly}\alpha, \text{b}}$ measurements with those in the four aforementioned LAEs with a blue bump to construct a large sample of LAEs with a blue bump consisting of 9 objects (10 spectra): one from McLinden et al. (2011) with $\Delta v_{\text{Ly}\alpha, \text{b}} = -454$ km s $^{-1}$ and three from Chonis et al. (2013) with $\Delta v_{\text{Ly}\alpha, \text{b}} = -127, -250, \text{ and } -236$ km s $^{-1}$. The mean $\Delta v_{\text{Ly}\alpha, \text{b}}$ value of the large sample is $\Delta v_{\text{Ly}\alpha, \text{b}} = -316 \pm 45$ km s $^{-1}$, which is consistent with that of 11 LBGs with a blue bump, $\Delta v_{\text{Ly}\alpha, \text{b}} = -367 \pm 46$ km s $^{-1}$ (Kulas et al. 2012). We calculate the K-S probability to be 0.3901, indicating that LAEs' $\Delta v_{\text{Ly}\alpha, \text{b}}$ values are comparable to LBGs'. The middle panel of Figure 3 shows the $\Delta v_{\text{Ly}\alpha, \text{b}}$ distri-

bution for the LAE and LBG samples.

We check if our conclusion remains unchanged even if the spectral resolution effect is taken into account. The sample by Kulas et al. (2012) has been obtained with three settings: 300-line grating, 400-, and 600-line grisms, corresponding to a spectral resolution of $R \sim 600, 800, \text{ and } 1300$, respectively. We compare the mean $\Delta v_{\text{Ly}\alpha, \text{b}}$ value of our four LAEs taken by LRIS ($R \sim 1100$) and that of six LBGs with a blue bump obtained at a similar resolution ($R \sim 1300$). The resultant mean $\Delta v_{\text{Ly}\alpha, \text{b}}$ values for LAEs and LBGs are -340 ± 99 and -356 ± 70 km s $^{-1}$, respectively, and the K-S probability is 0.9238. Thus, we obtain the same conclusion.

3.4.3. Velocity Offsets Between the Main Red Peak and the Blue Bump, Δv_{peak}

Finally, for each of the spectra with a blue bump, we measure the velocity offset between the red and blue peaks: $\Delta v_{\text{peak}} = 597 \pm 67$ km s $^{-1}$ (CDFS-3865), 414 ± 78 km s $^{-1}$ (MagE-COSMOS-43982), 776 ± 117 km s $^{-1}$ (COSMOS-12805), 405 ± 105 km s $^{-1}$ (COSMOS-13138), 320 ± 98 km s $^{-1}$ (LRIS-COSMOS-43982), and 556 ± 66 km s $^{-1}$ (SXDS-10942), as listed in the column 7 of Table 2. In order to make a large sample with Δv_{peak} measured, we utilize again the four LAEs with the blue bump from the literature: one LAE studied in McLinden et al. (2011) with $\Delta v_{\text{peak}} = 796$ km s $^{-1}$ and three LAEs studied in Chonis et al. (2013) with $\Delta v_{\text{peak}} = 300, 425, \text{ and } 415$ km s $^{-1}$. The mean value of the nine objects (ten spectra) is $\Delta v_{\text{peak}} = 500 \pm 56$ km s $^{-1}$, which is significantly smaller than the value derived for 11 LBGs with a blue bump, $\Delta v_{\text{peak}} = 801 \pm 41$ km s $^{-1}$ (Group I in Kulas et al. 2012). The K-S probability is calculated to be 0.00636, indicating that LAEs and LBGs have distinctive Δv_{peak} values. See the right panel of Figure 3 for their distributions.

We examine the spectral resolution effect exactly the same manner as in §3.4.2. The mean Δv_{peak} value of the four LAEs taken by LRIS ($R \sim 1100$) and that of the six LBGs with a blue bump obtained at a similar spectral resolution ($R \sim 1300$) are $\Delta v_{\text{peak}} = 514 \pm 100$ and 778 ± 59 km s $^{-1}$, respectively. In conjunction with the K-S probability, 0.09524, we conclude that LAEs have a significantly smaller Δv_{peak} value than that of LBG even at the same spectral resolution. Our finding is recently supported by Henry et al. (2015) and Yang et al. (2015), who have examined Ly α velocity properties and their relations to the Ly α escape fraction for local galaxies called ‘‘Green Peas’’ galaxies (Cardamone et al. 2009). They have found that the Ly α escape fraction is higher for

objects with smaller Δv_{peak} .

In summary, we have derived three Ly α velocity offsets, $\Delta v_{\text{Ly}\alpha, \text{r}}$, $\Delta v_{\text{Ly}\alpha, \text{b}}$, and Δv_{peak} . While we need a larger sample of objects with a blue bump for a definite conclusion, we find that LAEs have a smaller (comparable) $\Delta v_{\text{Ly}\alpha, \text{r}}$ ($\Delta v_{\text{Ly}\alpha, \text{b}}$) value relative to LBGs, which makes their Δv_{peak} value also smaller than that of LBGs.

3.5. Other Physical Quantities

In this section, we describe other physical quantities related to this work. We describe metal absorption line properties in §3.5.1, SED fitting properties in §3.5.2, and morphological properties in §3.5.3.

3.5.1. Metal Absorption Line Properties

Low ionization state (LIS) metal absorption lines encode information on cold neutral gas in galaxies. The mean blueshift of LIS absorption lines with respect to the systemic velocity, Δv_{abs} , gives the average speed of the galactic outflow (e.g., Pettini et al. 2001; Shapley et al. 2003; Martin 2005). In the following sections, we compare the Δv_{abs} values of our LAE sample with the results from Ly α radiation transfer fitting.

Shibuya et al. (2014b) have detected several LIS absorption lines in a few narrowband-selected LAEs on the individual basis. The derived mean blue shifts are $\Delta v_{\text{abs}} = -130 \pm 70 \text{ km s}^{-1}$ (COSMOS-13636), $-170 \pm 50 \text{ km s}^{-1}$ (COSMOS-12805), and $-260 \pm 60 \text{ km s}^{-1}$ (SXDS-10600). Additionally, Hashimoto et al. (2013) have detected several LIS absorption lines in a stacked spectrum of four LAEs: CDFS-3865, CDFS-6482, COSMOS-13636, and COSMOS-30679. The mean blueshift of the LIS metal absorption lines is $\Delta v_{\text{abs}} = -102 \pm 65 \text{ km s}^{-1}$. These values are listed in the column 2 of Table 4.

3.5.2. SED Fitting Properties

In this study, we utilize SED fitting results of the sample, in particular, stellar dust extinction, $E(B-V)_*$, and stellar mass, M_* . In the following sections, we compare the $E(B-V)_*$ values with the results from Ly α radiation transfer fitting, and investigate the correlation between the Ly α profile trends and M_* .

SED fitting results for the MagE (LRIS) objects have been presented in Hashimoto et al. (2013) and Nakajima et al. (2013) (Shibuya et al. 2014b). For the detail procedure of the fitting, we refer the reader to Ono et al. (2010a,b). The derived $E(B-V)_*$ and M_* values are listed in the columns 3 and 4 in Table 4. The former range from $E(B-V)_* = 0.04$ to 0.40 with a mean value of $E(B-V)_* = 0.16$, and the latter from $\log M_*/M_\odot = 7.7$ to 10.8 with a mean of $\log M_*/M_\odot = 9.3$, respectively.

3.5.3. Morphological Properties

In the following sections, we use three morphological properties studied for $z \sim 2.2$ LAEs in Shibuya et al. (2014a): the presence of a merger, the spatial offset between Ly α and stellar-continuum emission peaks, $\delta_{\text{Ly}\alpha}$, and the ellipticity. Shibuya et al. (2014a) have utilized I_{814} and H_{160} data taken with ACS and WFC3 on *HST* to examine rest-frame UV and optical morphologies, respectively. Among the objects presented in this study,

the rest-frame UV images of the eight COSMOS objects have been investigated in Shibuya et al. (2014a).

The presence of a merger has been examined with two methods: the close-pair method (e.g., Le Fèvre et al. 2000; Law et al. 2012) and the morphological index method, especially *CAS* system (Abraham et al. 1996; Conselice et al. 2000). In Shibuya et al. (2014a), the former method has been applied to objects with $I_{814} < 26.5$, which is the case for all the COSMOS objects presented in this study except for COSMOS-13138. The result is that two objects, COSMOS-13636 and COSMOS-12805, are mergers, while the remaining seven are not. On the other hand, the latter method has been done for objects with $I_{814} < 25.0$ and a half light radius, r_e , larger than $0.''09$. The reason why Shibuya et al. (2014a) have limited the sample for the latter method is to obtain reliable values of the indices. This is the case for three COSMOS objects presented in this study, COSMOS-13636, COSMOS-43982, and COSMOS-38380. The result is that none of the three is a merger. The two results for COSMOS-13636 are not consistent with each other because we have used two different methods. Thus, among the eight COSMOS objects, COSMOS-13636 and COSMOS-12805 may be a merger (the column 5 of Table 4).

The Ly α spatial offset, $\delta_{\text{Ly}\alpha}$, has been examined by performing source detections with **SExtractor** for Subaru NB387 and *HST* I_{814} images. While compact objects with a symmetric UV light profile tend to have a small $\delta_{\text{Ly}\alpha}$ value, objects with an asymmetric, disturbed UV light profile likely to have a large $\delta_{\text{Ly}\alpha}$ value (e.g., Jiang et al. 2013; Shibuya et al. 2014a). Thus, this quantity could be a useful tracer of the H I gas stability around the galaxy. The value is reliably obtained for the objects with $I_{814} < 26.5$ and NB387 < 24.5 , where the typical positional error in I_{814} (NB387) is less than $0.''02$ ($0.''3$). For the eight COSMOS objects in this study, none has a significant Ly α spatial offset larger than the typical error of the $\delta_{\text{Ly}\alpha}$, $\sim 0.''36$.

The ellipticity, $\epsilon = 1 - a/b$, where a and b are the major and minor axes, is a useful indicator of the galactic disk inclination. In Shibuya et al. (2014a), this has been measured using **GALFIT** software (Peng et al. 2002) for the objects with $I_{814} < 25.0$ and r_e larger than the typical PSF size. The former criterion, corresponding to $S/N = 30$ detection, is needed for the reliable ellipticity measurements (e.g., Mosleh et al. 2012; Ono et al. 2013). Only three objects, COSMOS-30679, COSMOS-38380, and COSMOS-43982, satisfy these criteria. The resultant ellipticity values are $\epsilon = 0.24$ (COSMOS-30679), 0.34 (COSMOS-38380), and 0.49 (AGN-COSMOS-43982), respectively (the column 6 of Table 4).

4. LY α RADIATIVE TRANSFER MODEL AND FITTING PROCEDURE

4.1. A Library of Synthetic Spectra

The library of synthetic Ly α spectra used in this study has been described in Schaerer et al. (2011). Ly α radiation transfer has been computed with **McLya** (Verhamme et al. 2006) through spherically symmetric expanding shells of homogeneous and isothermal neutral hydrogen gas. The shell is describe by four parameters:

- the radial expansion velocity, V_{exp} ,

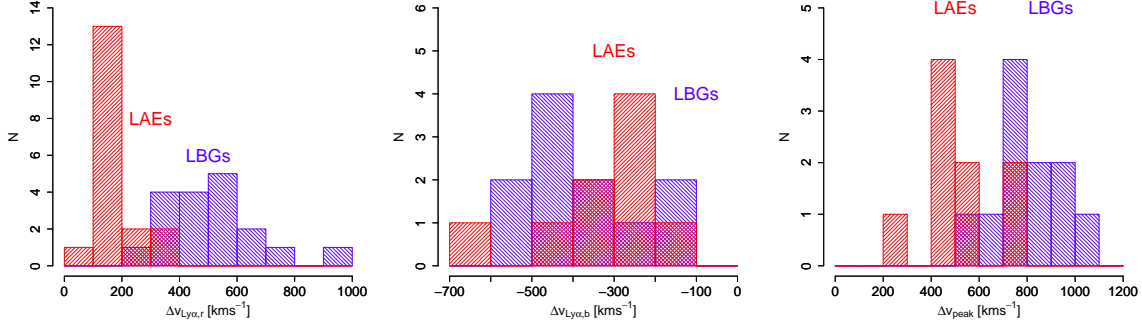


FIG. 3.— Histograms of $\Delta v_{\text{Ly}\alpha, r}$ (left panel), $\Delta v_{\text{Ly}\alpha, b}$ (middle), and Δv_{peak} (right) for the LAEs studied in this paper and the literature (McLinden et al. 2011; Chonis et al. 2013) and LBGs given by Kulas et al. (2012).

TABLE 4
SUMMARY OF THE OTHER PHYSICAL PROPERTIES

Object	Δv_{abs}	$\log(M_*)$	$E(B - V)_*$	merger (pair, <i>CAS</i>)	ϵ
(1)	(km s^{-1}) (2)	(M_\odot) (3)	(mag.) (4)	(5)	(6)
CDFS-3865	(-102 ± 65)	$9.50^{+0.01}_{-0.03}$	$0.14^{+0.00}_{-0.00}$	-, -	-
CDFS-6482	(-102 ± 65)	$9.80^{+0.06}_{-0.05}$	$0.15^{+0.02}_{-0.02}$	-, -	-
COSMOS-08501	-	$7.84^{+1.21}_{-0.27}$	$0.08^{+0.04}_{-0.08}$	no, -	-
COSMOS-30679	(-102 ± 65)	$9.74^{+0.26}_{-0.52}$	$0.24^{+0.04}_{-0.04}$	no, -	0.24
COSMOS-13636	-130 ± 70 (-102 ± 65)	$9.12^{+0.13}_{-0.14}$	$0.18^{+0.01}_{-0.01}$	yes, no	-
COSMOS-43982	-	$10.80^{+0.01}_{-0.06}$	$0.40^{+0.00}_{-0.00}$	no, no	0.49
COSMOS-08357	-	$9.21^{+0.28}_{-0.40}$	$0.14^{+0.05}_{-0.05}$	no, -	-
COSMOS-12805	-170 ± 50	$9.44^{+0.13}_{-0.17}$	$0.16^{+0.02}_{-0.02}$	yes, -	-
COSMOS-13138	-	$9.48^{+0.22}_{-0.20}$	$0.19^{+0.04}_{-0.04}$	-, -	-
COSMOS0-38380	-	$10.06^{+0.06}_{-0.11}$	$0.13^{+0.02}_{-0.01}$	no, no	0.34
SXDS-10600	-260 ± 60	$9.46^{+0.05}_{-0.04}$	$0.05^{+0.00}_{-0.01}$	-, -	-
SXDS-10942	-	$7.73^{+0.11}_{-0.08}$	$0.04^{+0.02}_{-0.02}$	-, -	-

NOTE. — The symbol “-” indicates no measurement. (1) Object ID; (2) Mean velocity offset of LIS absorption lines with respect to z_{sys} ; (3) Stellar mass estimated from SED fitting; (4) Stellar dust extinction estimated from SED fitting; (5) Presence of merger examined via close-pair method and *CAS* system studied in Shibuya et al. (2014a); (6) Ellipticity defined as $\epsilon = 1 - b/a$, where a and b are the major and minor axes, respectively.

- the neutral hydrogen column density along the line of sight, N_{HI} ,
- the Doppler parameter, b , describing the thermal and turbulent motion in the shell,
- and the dust absorption optical depth at the Ly α wavelength, τ_a , related to the gas dust extinction by $E(B - V)_{\text{gas}} \approx (0.06 \dots 0.11) \tau_a$, where the lower and higher values in the parenthesis correspond to the attenuation law for starbursts (Calzetti et al. 2000) and the Galactic extinction law (Seaton 1979), respectively.

The Ly α source is located at the center of the shell. The intrinsic (i.e., before being affected by the radiative transfer effect) spectrum is a Gaussian Ly α line plus a flat continuum, and is characterized by two parameters :

- the Ly α equivalent width, $\text{EW}_{\text{int}}(\text{Ly}\alpha)$,
- and the full width at half maximum, $\text{FWHM}_{\text{int}}(\text{Ly}\alpha)$.

For a comparison with the observed data, each rest-frame model has been shifted using the systemic redshift z_{sys} values listed in Table 2. To reflect the z_{sys} uncertainty, we have allowed the observed Ly α spectra to shift relative to the velocity zero point within the error. Thus, combinations of seven free parameters are fitted to the data.

This library of Ly α spectra has been successfully used to reproduce various observed Ly α line profiles of $z > 3$ LBGs, from strong emission to broad absorption (Verhamme et al. 2008; Schaerer & Verhamme 2008; Dessauges-Zavadsky et al. 2010; Vanzella et al. 2010; Lidman et al. 2012).

4.2. Fitting of Observed Spectra

To perform a statistical comparison between the observed and modeled Ly α line profiles, we calculate the χ^2 values for each of the possible combinations of the parameters for each galaxy (cf., Chonis et al. 2013). Since model spectra are normalized and at an infinite spectral resolution, two steps are needed before the χ^2 calculation. First, we normalize the observed spectra using the

continuum level estimated at wavelengths longer than 1216Å. Second, each model Ly α spectrum has been convolved with a Gaussian whose FWHM corresponds to spectral resolutions:

$$\text{FWHM} = c/R, \quad (4)$$

where c is the speed of light.

We note that our fitting technique gives exactly the same statistical weight to all data points of the continuum and the Ly α line. Finally for the sake of consistency, for each object we calculate χ^2 in the wavelength range from $-3 \times \text{FWHM}_{\text{obs}}(\text{Ly}\alpha)$ to $+3 \times \text{FWHM}_{\text{obs}}(\text{Ly}\alpha)$ around the Ly α line center.

In Figure 4, we demonstrate how the best fit, and its associated errors, are found using χ^2 values. To do this, examples of the fit to V_{exp} are shown for well and poorly constrained objects. In the left panels of this figure, one can see a broad range of V_{exp} values with low reduced χ^2 for COSMOS-08357 whose Ly α S/N ratio is ~ 11 , in comparison to CDFS-3865 with a Ly α S/N of ~ 98 . To measure median and 1σ values, we convert χ^2 values into probabilities using the formula, $p \propto \exp(-\chi^2/2)$ for each five 2D parameter set (V_{exp} vs. N_{HI} , V_{exp} vs. τ_a , V_{exp} vs. b , V_{exp} vs. $\text{FWHM}_{\text{int}}(\text{Ly}\alpha)$, and V_{exp} vs. $\text{EW}_{\text{int}}(\text{Ly}\alpha)$). After normalizing them so that the total probability is unity, we draw a probability (PDF) and a cumulative density function (CDF) as shown in the middle and the right panels, respectively. Finally, we adopt the values where the CDF value satisfying $\text{CDF} = 0.50, 0.16$, and 0.84 as the median and $\pm 1\sigma$, respectively. Performing this for each five 2D parameter set results in five median and $\pm 1\sigma$ values. As can be seen, all the five median and $\pm 1\sigma$ values are consistent with each other for CDFS-3865, whereas those are not for COSMOS-08357. In the latter case, we adopt the average of the five median and $\pm 1\sigma$ values.

4.3. Results

We show the reproduced Ly α profiles (§4.3.1), describe the derived parameters (§4.3.2), and examine the influence of spectral resolution on the results (§4.3.3).

4.3.1. Fitted Profiles

Figure 5 shows the best fit model spectra with the observed ones. All the Ly α profiles are quite well reproduced by the model, which seems to differ from the previous studies by Kulas et al. (2012) and Chonis et al. (2013). These authors have had difficulty reproducing their Ly α profiles, especially the position and the flux of the blue bump. This might be due to model differences. These two studies have utilized the uniform expanding shell model constructed by Zheng & Miralda-Escudé (2002) and Kollmeier et al. (2010). There are three major differences between the models (c.f., Chonis et al. 2013). First, in addition to the three common parameters, V_{exp} , N_{HI} , and b , the model used in this study also includes an additional one for dust absorption. Second, the grid points and the physical range of parameters are different. The model by Zheng & Miralda-Escudé (2002) and Kollmeier et al. (2010) has four values for each parameter: $V_{\text{exp}} = 50, 100, 200, 300 \text{ km s}^{-1}$, $\log(N_{\text{HI}}) = 17, 18, 19, 20.3 \text{ cm}^{-2}$, and $b = 20, 40, 80, 120 \text{ km s}^{-1}$, whereas the model used in this study has 12 V_{exp} ,

13 N_{HI} , and 5 b values spanning wider physical ranges. Finally, the intrinsic spectrum of the previous models is a monochromatic Ly α line, while we model a Gaussian Ly α plus a continuum. As we show in §4.3.2 and later sections, we infer that the key to better reproducing the blue bump is to assume the Ly α profile to be a (broad) Gaussian.

4.3.2. Derived Parameters

The best fit parameters are summarized in Table 5. We describe the mean values of the derived parameters, and systematically compare them with those of LBGs modeled by the same code (Verhamme et al. 2008; Schaerer & Verhamme 2008; Dessauges-Zavadsky et al. 2010). For the parameter $\text{FWHM}_{\text{int}}(\text{Ly}\alpha)$, we examine the mean values of two subsamples, objects with a blue bump and those without. We have checked that there is no significant difference between the two subsamples in the other parameters.

The mean V_{exp} value of the LAEs is $148 \pm 14 \text{ km s}^{-1}$, which is comparable to that of LBGs, $131 \pm 25 \text{ km s}^{-1}$. This strongly disfavors the hypothesis that the small $\Delta v_{\text{Ly}\alpha}$ of LAEs is due to their large outflow velocity.

The most interesting parameter, N_{HI} , ranges from $\log(N_{\text{HI}}) = 16.0$ to 19.7 cm^{-2} , with a mean value of $18.4 \pm 0.4 \text{ cm}^{-2}$, which is more than one order of magnitude smaller than the typical $\log(N_{\text{HI}})$ value of LBGs, $19.8 \pm 0.2 \text{ cm}^{-2}$.

The mean values of τ_a and b are 0.9 ± 0.2 and $37 \pm 10 \text{ km s}^{-1}$, respectively, both of which are comparable to those of LBGs, 0.8 ± 0.1 and $28 \pm 5 \text{ km s}^{-1}$.

$\text{FWHM}_{\text{int}}(\text{Ly}\alpha)$ values range from $\text{FWHM}_{\text{int}}(\text{Ly}\alpha) = 50$ to 847 km s^{-1} . The mean values for the whole sample, the non blue bump sample, and the blue bump sample, are $354, 169$, and 602 km s^{-1} , respectively. This shows that the blue bump objects have significantly larger $\text{FWHM}_{\text{int}}(\text{Ly}\alpha)$ than that found in the non blue bump objects. This trend is similar to Verhamme et al. (2008); They have found that most LBGs with a single peaked Ly α profile are best fitted with moderate values of $\text{FWHM}_{\text{int}}(\text{Ly}\alpha)$, $\sim 200 \text{ km s}^{-1}$, whereas the best fit $\text{FWHM}_{\text{int}}(\text{Ly}\alpha)$ values for two LBGs with a blue bump are greater than 500 km s^{-1} . These results support our claim that large $\text{FWHM}_{\text{int}}(\text{Ly}\alpha)$ helps fitting the blue bump. We investigate if there are any observational trends for the blue bump objects, and discuss possible mechanisms for the blue bump objects to have large $\text{FWHM}_{\text{int}}(\text{Ly}\alpha)$ in §5.1.

Since starburst activities that produce Ly α photons should be similar between LAEs and LBGs, we expect comparable $\text{EW}_{\text{int}}(\text{Ly}\alpha)$ values for these two galaxy populations. The result is that the mean $\text{EW}_{\text{int}}(\text{Ly}\alpha)$ value of LAEs, $65 \pm 18 \text{ Å}$, is somewhat smaller than that of LBGs, $107 \pm 25 \text{ Å}$.

In summary, the model parameter N_{HI} derived in LAEs is more than one order of magnitude smaller than that of LBGs, whereas the remaining parameters are consistent within 1σ between LAEs and LBGs.

4.3.3. Influence of Spectral Resolution on the Fitting Procedure

To investigate the influence of spectral resolution on the fitting results, we compare the best fit parameters

of the two objects observed with the two spectrographs, COSMOS-13636 and COSMOS-43982. As can be seen in Table 5, the two fitting results of COSMOS-43982 are consistent with each other, whereas those of COSMOS-13636 are not, possibly owing to the large difference in the best-fit reduced χ^2 , 1.1 and 6.2.

Taking a closer look into these two fits, we see that the extremely small 1σ noise in the flux of LRIS-COSMOS-13636 could be a key reason for its high χ^2 value. On the other hand, the modeled spectrum seems to be over-smoothed, leading us to infer its Ly α line resolution is under-estimated. Indeed, it is known that the spectral resolution for a given line can be higher than the canonical value. A combination of these factors would naturally cause the large resultant χ^2 value, and the discrepancy between the different best-fit parameters at two resolutions.

4.4. Degeneracy among Parameters

In this subsection, we investigate degeneracies among the model parameters to understand how they affect our determination of the best fit parameters. First we describe possible degeneracies and then statistically examine them using 2D χ^2 values.

It is possible that parameters τ and $\text{EW}_{\text{int}}(\text{Ly}\alpha)$ are degenerated as an observed profile can be reproduced equivalently well either assuming a weak intrinsic line with low dust extinction, or a strong intrinsic line with high dust extinction. There would also be a degeneracy between b and $\text{FWHM}_{\text{int}}(\text{Ly}\alpha)$ in the sense that both broaden the line profile. Furthermore, when there is a blue bump in the profile, we need either a high b or a low V_{exp} to reproduce it.

Figures 13 - 15 in the Appendix are 2D parameter grid maps for CDFS-3865 with the grey dots showing the entire grids. We use these maps and χ^2 values to examine the actual degeneracies among the parameters. If there is a degeneracy between two parameters, the χ^2 contour would be tilted and elongated. The blue grids in these figures show those satisfying $\Delta\chi^2 \leq 6.17$ above the raw minimum χ^2 designated by the white dots, i.e., the 3σ uncertainty in the parameter set (Press et al. 1992). Thanks to the number of data points given by high spectral resolutions, and the relatively coarse grids, even the 3σ uncertainty is converged into one grid. This indicates that there is no degeneracy that affects our determination of the best fit. We have checked that this is also true for the rest of the sample in this study. Thus, we conclude that the systematic uncertainties among the parameters due to the degeneracies are small, and thus do not affect our discussions.

4.5. Comparison between Observation and Model

In order to examine if the best fit parameters are reasonable, we compare the derived parameters with the observables.

4.5.1. $|\Delta v_{\text{abs}}|$ vs. V_{exp}

As stated in §3.5.1, several LIS absorption lines have been detected in individual spectra of COSMOS-12805, COSMOS-13636, and SXDS-10600 (Shibuya et al. 2014b), and in a stacked spectrum of four LAEs, CDFS-3865, CDFS-6482, COSMOS-13636, and COSMOS-30679 (Hashimoto et al. 2013). The measured blueshift

of LIS absorption lines with respect to the systemic, Δv_{abs} , is listed in Table 4. Figure 6 shows a comparison between $|\Delta v_{\text{abs}}|$ and the best-fit expansion velocity, V_{exp} . For the stacked spectrum, we plot the mean V_{exp} value of the four LAEs, $163 \pm 25 \text{ km s}^{-1}$. While there are only four data points, $|\Delta v_{\text{abs}}|$ and V_{exp} are in excellent agreement with each other.

4.5.2. $E(B-V)_*$ vs. τ_a

The stellar dust extinction values, $E(B-V)_*$, for the sample have been derived in previous studies (Hashimoto et al. 2013; Nakajima et al. 2013; Shibuya et al. 2014b) (see §3.5.1). Figure 7 compares them with gas dust extinction, $E(B-V)_{\text{gas}}$, derived assuming the relation:

$$E(B-V)_{\text{gas}} \approx 0.10\tau_a. \quad (5)$$

Dotted and dashed lines correspond to empirical relations $E(B-V)_* = E(B-V)_{\text{gas}}$ (Erb et al. 2006a) and $E(B-V)_* = 0.44E(B-V)_{\text{gas}}$ (Calzetti et al. 2000), respectively, for *host galaxies*. As Kashino et al. (2013) have shown, the difference between $E(B-V)_*$ and $E(B-V)_{\text{gas}}$ becomes smaller for higher- z galaxies.

In this study, we expect that data points are located below these relations. This is because $E(B-V)_{\text{gas}}$ obtained from Ly α modeling is gas dust extinction for *out-flowing shells*, which should be smaller than that for *host galaxies*. The figure shows that half of the sample roughly lie between the two lines, while the rest of the sample show low $E(B-V)_{\text{gas}}$ values. A similar trend has been found in Figure 12 of Verhamme et al. (2008) who have compared $E(B-V)_*$ and $E(B-V)_{\text{gas}}$ for $z \sim 3$ LBGs. They have assumed two different star formation histories (SFHs) in deriving $E(B-V)_*$: a constant SFH indicated by red triangles and an exponentially decreasing SFH indicated by blue open circles, the former of which is the same as that assumed in this study. Both our data and the red triangles in Verhamme et al. (2006) are similarly distributed in the sense that half of the sample has comparable extinction values and the rest has low $E(B-V)_{\text{gas}}$ values.

4.5.3. $\text{FWHM}(\text{neb})$ vs. $\text{FWHM}_{\text{int}}(\text{Ly}\alpha)$

Figure 8 plots the observed FWHM of nebular emission lines, $\text{FWHM}(\text{neb})$, versus modeled FWHM of the intrinsic (i.e., before being affected by the radiative transfer effect) Ly α line, $\text{FWHM}_{\text{int}}(\text{Ly}\alpha)$. Assuming that both Ly α and nebular emission lines originate from HII regions, the two FWHMs should be similar. However, $\text{FWHM}_{\text{int}}(\text{Ly}\alpha)$ is systematically larger than $\text{FWHM}(\text{neb})$. Additional scattering of Ly α photons in an HII region due to residual H I atoms in it may be at work. Assuming a static HII region with a neutral hydrogen column density of $\log(N_{\text{HI}}) \lesssim 17.0 \text{ cm}^{-2}$, corresponding to an unity optical depth for ionizing photons, $\tau_{\text{ion}} \lesssim 1$ (cf., Verhamme et al. 2015), $\text{FWHM}_{\text{int}}(\text{Ly}\alpha)$ can be broadened by 200 km s^{-1} compared to $\text{FWHM}(\text{neb})$. As can be seen from Figure 8, while this additional broadening would help explain the discrepancy for the non blue bump objects, it is still not enough for the blue bump objects. We discuss some interpretations for the huge $\text{FWHM}_{\text{int}}(\text{Ly}\alpha)$ in the blue bump objects in §5.1.

We also perform Ly α profile fitting of the blue bump objects with fixing $\text{FWHM}_{\text{int}}(\text{Ly}\alpha) = \text{FWHM}(\text{neb})$. As

TABLE 5
SUMMARY OF THE LY α FITTING FOR THE SAMPLE

Object	χ^2_{red}	V_{exp} (km s $^{-1}$)	$\log(N_{\text{HI}})$ (cm $^{-2}$)	τ_a	b (km s $^{-1}$)	FWHM(Ly α) $_{\text{int.}}$ (km s $^{-1}$)	EW(Ly α) $_{\text{int.}}$ (Å)
(1)	(2)	(3)	(4)	(5)	(6)	(7)	(8)
CDFS-3865	3.1	120 $^{+21}_{-14}$	19.5 $^{+0.1}_{-0.1}$	0.0 $^{+0.0}_{-0.0}$	15 $^{+13}_{-5}$	846 $^{+106}_{-97}$	35 $^{+7}_{-7}$
CDFS-6482	1.3	177 $^{+18}_{-18}$	19.2 $^{+0.1}_{-0.1}$	0.12 $^{+0.04}_{-0.08}$	10 $^{+8}_{-0}$	271 $^{+38}_{-29}$	28 $^{+0}_{-7}$
COSMOS-08501	1.3	167 $^{+286}_{-106}$	18.7 $^{+0.5}_{-1.1}$	1.56 $^{+1.54}_{-1.07}$	13 $^{+14}_{-3}$	252 $^{+240}_{-134}$	14 $^{+7}_{-7}$
COSMOS-30679	1.0	127 $^{+14}_{-21}$	19.5 $^{+0.1}_{-0.1}$	1.43 $^{+1.03}_{-0.53}$	29 $^{+8}_{-8}$	50 $^{+38}_{-0}$	39 $^{+1}_{-11}$
COSMOS-13636 (MagE)	1.1	226 $^{+14}_{-21}$	16.0 $^{+0.0}_{-0.0}$	0.12 $^{+0.14}_{-0.08}$	121 $^{+27}_{-27}$	256 $^{+101}_{-58}$	28 $^{+0}_{-7}$
COSMOS-13636 (LIRS)	6.2	127 $^{+14}_{-21}$	18.8 $^{+0.2}_{-0.2}$	0.08 $^{+0.08}_{-0.04}$	30 $^{+8}_{-6}$	127 $^{+19}_{-19}$	28 $^{+0}_{-7}$
COSMOS-43982 (MagE)	1.0	141 $^{+88}_{-57}$	18.2 $^{+0.6}_{-1.6}$	1.15 $^{+1.54}_{-0.89}$	12 $^{+11}_{-2}$	544 $^{+120}_{-134}$	28 $^{+7}_{-11}$
COSMOS-43982 (LRIS)	1.4	138 $^{+85}_{-71}$	18.1 $^{+0.4}_{-1.5}$	0.02 $^{+0.22}_{-0.02}$	13 $^{+8}_{-3}$	621 $^{+53}_{-86}$	42 $^{+7}_{-7}$
COSMOS-08357	1.3	170 $^{+25}_{-42}$	19.7 $^{+0.1}_{-0.6}$	2.24 $^{+1.25}_{-0.95}$	19 $^{+14}_{-9}$	74 $^{+82}_{-24}$	85 $^{+42}_{-35}$
COSMOS-12805	3.1	177 $^{+18}_{-21}$	19.2 $^{+0.1}_{-0.1}$	1.73 $^{+0.71}_{-0.38}$	10 $^{+18}_{-0}$	645 $^{+38}_{-38}$	42 $^{+7}_{-0}$
COSMOS-13138	1.5	21 $^{+481}_{-21}$	18.8 $^{+0.4}_{-0.7}$	1.13 $^{+1.45}_{-0.89}$	15 $^{+14}_{-5}$	501 $^{+144}_{-144}$	64 $^{+11}_{-11}$
COSMOS-38380	2.1	127 $^{+14}_{-21}$	19.7 $^{+0.1}_{-0.1}$	0.69 $^{+0.28}_{-0.32}$	60 $^{+14}_{-14}$	99 $^{+9}_{-9}$	276 $^{+14}_{-21}$
SXDS-10600	6.2	226 $^{+14}_{-21}$	16.0 $^{+0.0}_{-0.0}$	1.74 $^{+0.20}_{-0.16}$	121 $^{+27}_{-27}$	223 $^{+19}_{-19}$	113 $^{+7}_{-7}$
SXDS-10942	1.6	131 $^{+32}_{-35}$	16.0 $^{+0.0}_{-0.0}$	0.12 $^{+0.08}_{-0.08}$	60 $^{+14}_{-14}$	453 $^{+82}_{-67}$	85 $^{+14}_{-7}$

NOTE. — (1) Object ID; (2) Reduced χ^2 value of the fitting calculated as $\chi^2_{\text{red}} = \chi^2/(N - M)$, where N and M denote the number of data points and the degree of freedom, respectively; (3) – (8) Best fit values of the radial expansion velocity, the column density of the neutral Hydrogen, the dust absorption optical depth, the Doppler parameter, the intrinsic Ly α FWHM, and the intrinsic Ly α EW, respectively.

shown in Figure 9, the blue bumps are poorly reproduced compared to the fitting without fixing FWHM $_{\text{int}}(\text{Ly}\alpha)$. We examine if the derived best-fit model parameters differ between the free and fixed FWHM $_{\text{int}}(\text{Ly}\alpha)$ cases. While there is no systematic difference for V_{exp} and N_{HI} , we find that b (τ_a) becomes large (small) in the fixed FWHM $_{\text{int}}(\text{Ly}\alpha)$ case. This would be related to the intrinsic degeneracy between them discussed in §4.4.

4.5.4. $EW(\text{Ly}\alpha)$ vs. $EW_{\text{int}}(\text{Ly}\alpha)$

Figure 10 plots the observed $EW(\text{Ly}\alpha)$ against the best fit intrinsic $EW(\text{Ly}\alpha)$ obtained from the Ly α fitting, $EW_{\text{int}}(\text{Ly}\alpha)$. Since we have modeled Ly α emission lines that fall in the slit, we use $EW(\text{Ly}\alpha)$ values measured from spectra as the observed $EW(\text{Ly}\alpha)$. All the data points are expected to lie above the one-to-one relation, $EW_{\text{int}}(\text{Ly}\alpha) \gtrsim EW(\text{Ly}\alpha)_{\text{spec}}$. This is because we have used the uniform shell model which does not boost $EW(\text{Ly}\alpha)$ unlike clumpy shell models (cf., Neufeld 1991; Laursen et al. 2013; Duval et al. 2014; Gronke & Dijkstra 2014). As can be seen, all the data points satisfy the expectation within the 1σ uncertainty.

5. DISCUSSION

5.1. *Mystery of the Blue Bump Objects*

As described in previous sections, FWHM $_{\text{int}}(\text{Ly}\alpha) > \text{FWHM}(\text{neb})$ is required to well reproduce the Ly α profiles with the blue bump objects. As seen in Figure 9, the

position and flux of the blue bump are poorly reproduced if we fix FWHM $_{\text{int}}(\text{Ly}\alpha) = \text{FWHM}(\text{neb})$.

In this section, we first examine if there are any characteristic properties for the blue-bump objects, and discuss the origin of the large discrepancy between the two FWHMs.

5.1.1. *Any Difference in Properties between the Blue Bump and the Non Blue Bump Objects?*

In §4.3.2, we have argued that, among the model parameters, only FWHM $_{\text{int}}(\text{Ly}\alpha)$ is significantly different between the blue-bump objects and the non blue-bump objects. Here we examine the difference in stellar mass, Ly α luminosity, morphological ellipticity, and the merger fraction between the two samples.

First, it is possible that the non blue bump objects have faint Ly α luminosities and/or small stellar masses so that the blue bump can not be observed. The Ly α luminosity of the blue bump sample ranges from $L(\text{Ly}\alpha) = 0.3$ to $29.8 \times 10^{42} \text{ erg s}^{-1}$ with a mean value of $8.8 \pm 5.6 \times 10^{42} \text{ erg s}^{-1}$, whereas that of the non-blue bump sample ranges from $L(\text{Ly}\alpha) = 0.5$ to $15.4 \times 10^{42} \text{ erg s}^{-1}$ with a mean value of $7.0 \pm 2.1 \times 10^{42} \text{ erg s}^{-1}$. This indicates that the two subsamples have similar Ly α luminosities. Likewise, the stellar mass of the blue bump sample ranges from $\log(M_*/M_\odot) = 7.73$ to 10.80, with a mean value of 9.4 ± 0.5 , whereas that of the non-blue bump sample ranges from $\log(M_*/M_\odot) = 7.84$ to 10.06, with a mean value of 9.3 ± 0.3 . Thus, this possibility is unlikely.

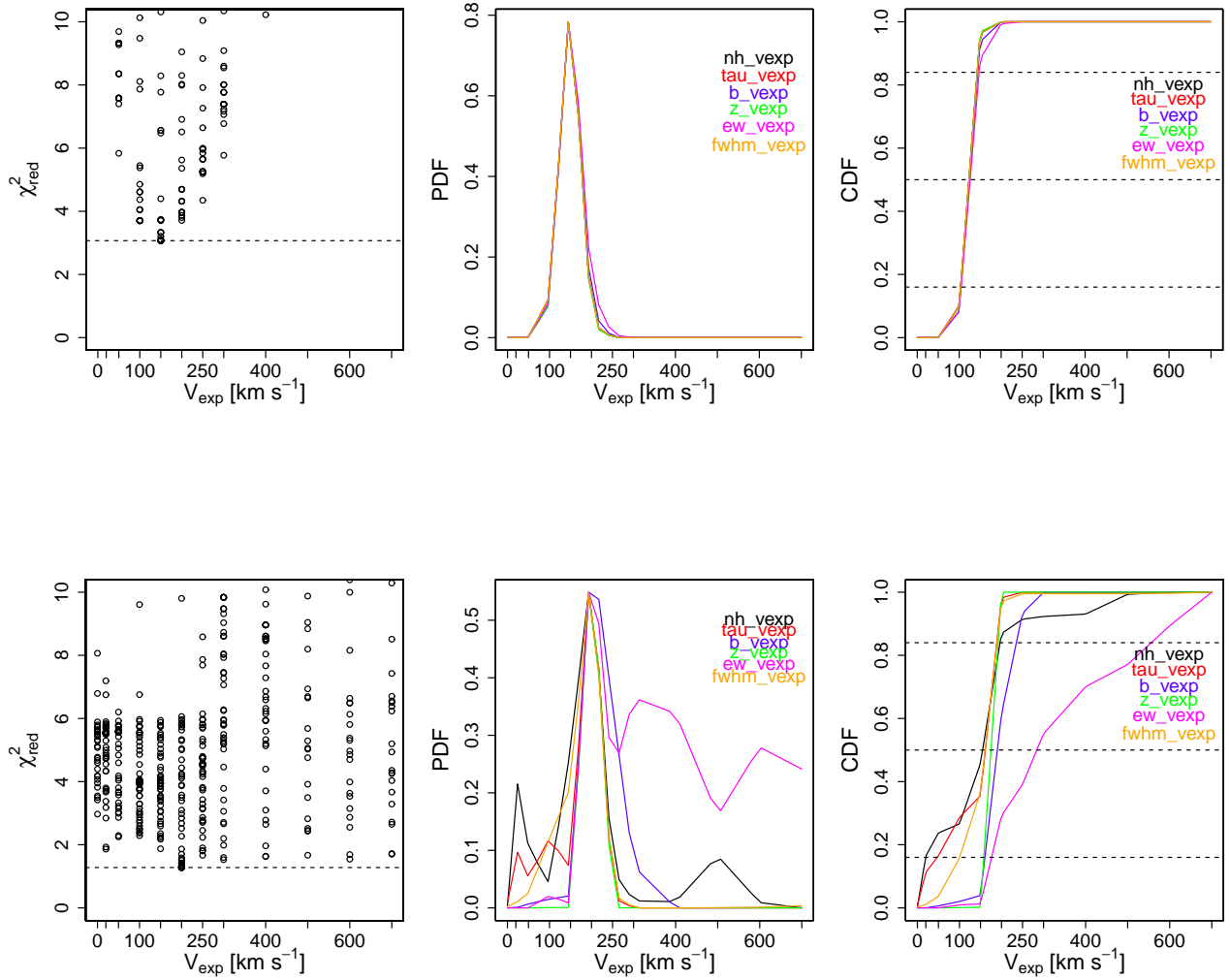


FIG. 4.— Examples of reduced χ^2 values (left panels), converted probability density functions (PDF) (middle panels), and cumulative density functions (CDF) (right panels), for the parameter V_{exp} . The upper (lower) panels are for CDFS-3865 (COSMOS-08357).

Second, objects with a blue bump may be more likely to be seen edge-on than those without. Recent theoretical studies (Verhamme et al. 2012; Zheng & Wallace 2014) have investigated the inclination effects to the Ly α emissivity and profile. These studies have shown that the blue bump flux relative to the total Ly α flux is enhanced with an increasing ellipticity. Indeed, Ly α profiles seen edge-on in these simulations resemble those produced by the static case of the spherical shell model. This is because outflowing gas is more likely to be blown out perpendicular to the galaxy disk, reducing the relative outflow velocity in the plane of the disk. As seen in Table 4, there are three objects whose ellipticity has been measured. Due to the small number of objects, we cannot determine if there is any difference between the two sub-samples.

Finally, as discussed in Kulas et al. (2012) and Chonis et al. (2013), galaxy merging can be the origin of the blue bump. In this case, the redder and bluer Ly α

emission components correspond to the two objects, respectively (see also Cooke et al. 2010; Rauch et al. 2011). However, as described in §3.5.3 (Table 4), the merger fraction in our sample is quite low.

We note here the observational results of Erb et al. (2010) and Heckman et al. (2011). These studies have found that objects with a blue bump tend to have a low covering fraction of the neutral gas measured by LIS absorption lines. Unfortunately, we cannot test this trend with our sample because of a too small number of objects with detection of LIS absorption lines.

We conclude that there is no significant difference in Ly α luminosity, stellar mass, morphological ellipticity, or the merger fraction between the two samples. A large sample, whose Ly α and absorption line velocity properties as well as morphological and stellar population properties are simultaneously available, is needed to understand the origin of blue bumps.

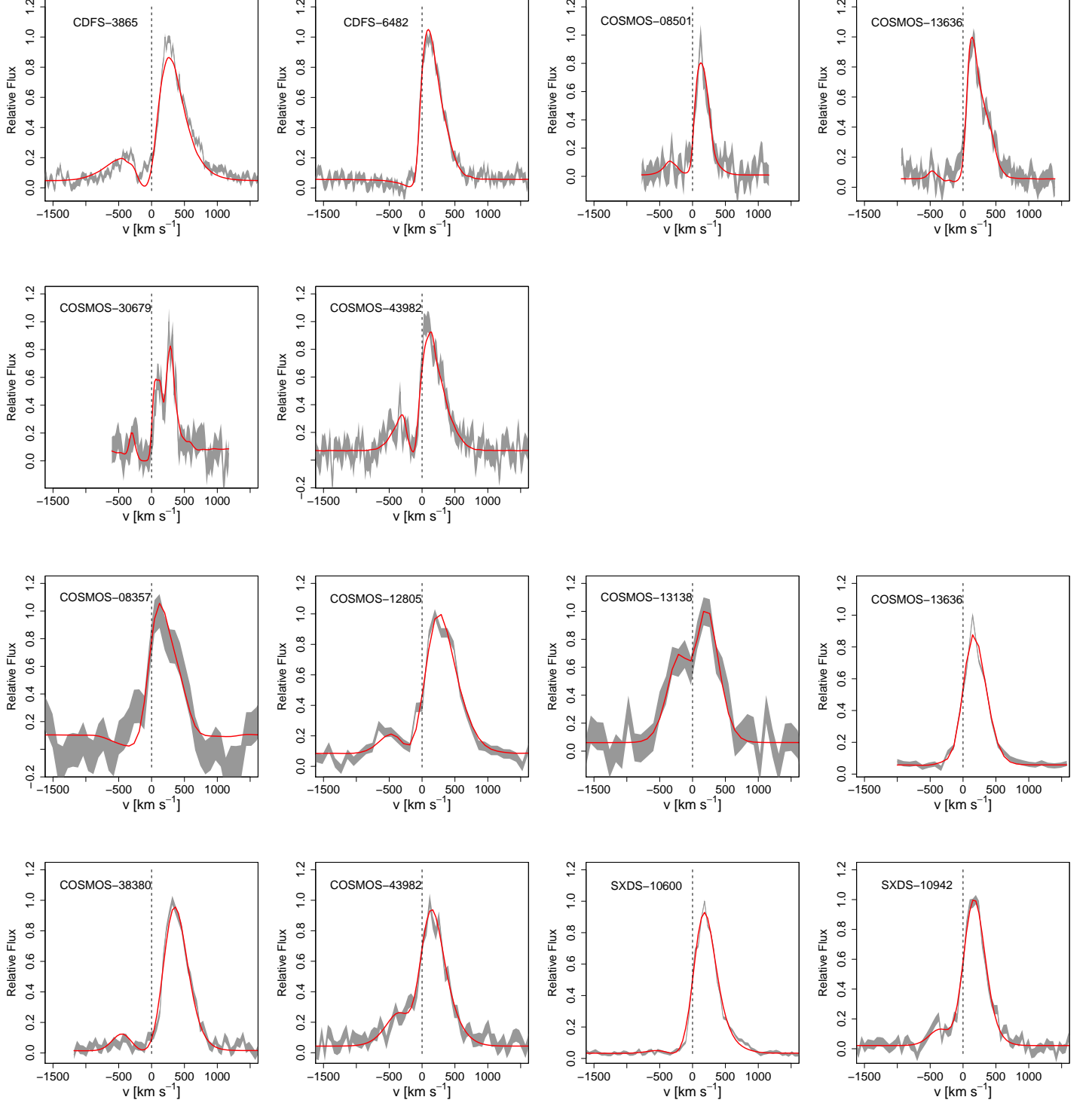


FIG. 5.— The upper two rows of panels show the reproduced $\text{Ly}\alpha$ line profiles (red) on top of the observed ones (grey) for the MagE objects, while the lower two rows of panes are those for the LRIS objects. The gray region denotes the 1σ range of the observed spectrum. All spectra are scaled to the wavelength range from -1500 to $+1500 \text{ km s}^{-1}$.

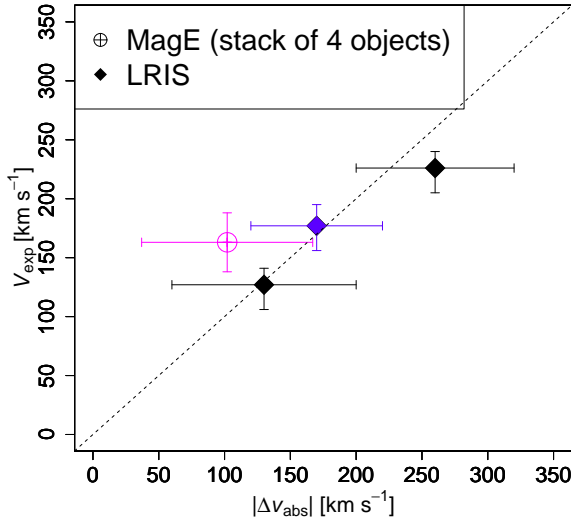


FIG. 6.— V_{exp} plotted against $|\Delta v_{\text{abs}}|$. The diamonds are the three LRIS objects whose LIS absorption lines are detected in the individual spectrum (Shibuya et al. 2014b). Blue color shows an object with a blue bump in the $\text{Ly}\alpha$ profile, while black color denotes those without. The magenta circle is the stacked spectrum of the four MagE LAEs, CDFS-3865, CDFS-6482, COSMOS-13636, and COSMOS-30679 (Hashimoto et al. 2013).

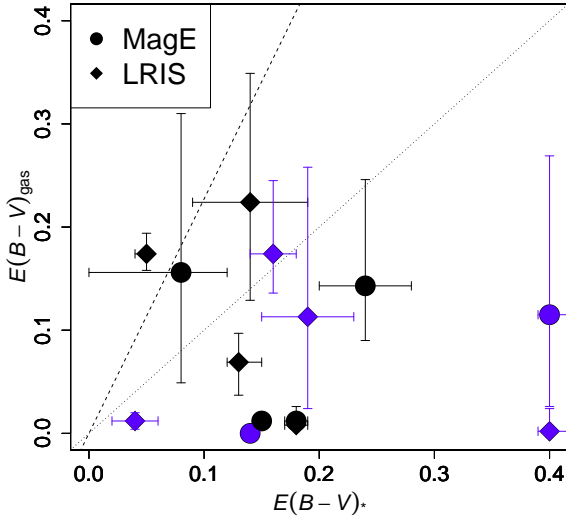


FIG. 7.— $E(B - V)_{\text{gas}}$ plotted against $E(B - V)_*$ for all the sample. The circles show the MagE objects, while the diamonds are the LRIS objects. Blue color shows objects with a blue bump in the $\text{Ly}\alpha$ profile, while black color denotes those without. The dotted and dashed lines correspond to $E(B - V)_* = E(B - V)_{\text{gas}}$ (Erb et al. 2006b) and $E(B - V)_* = 0.44E(B - V)_{\text{gas}}$ (Calzetti et al. 2000), respectively.

5.1.2. A Possible Explanation for Large $\text{FWHM}_{\text{int}}(\text{Ly}\alpha)$ in Blue Bump Objects

In this subsection, we explore a possible explanation of the large discrepancy between $\text{FWHM}_{\text{int}}(\text{Ly}\alpha)$ and $\text{FWHM}(\text{neb})$ in the blue bump objects.

It is possible that observed $\text{Ly}\alpha$ photons are pro-

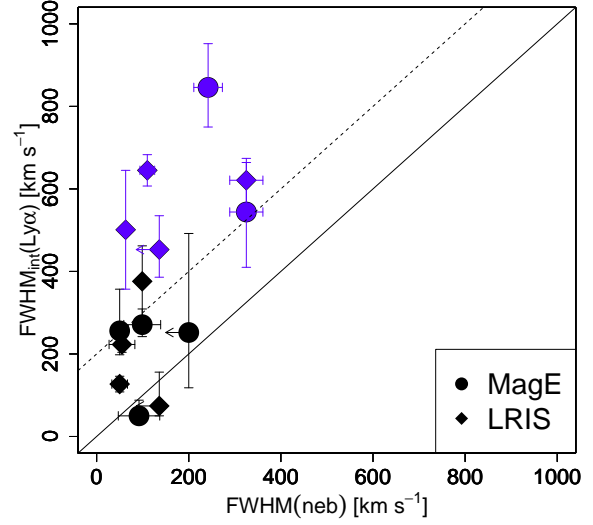


FIG. 8.— $\text{FWHM}_{\text{int}}(\text{Ly}\alpha)$ plotted against $\text{FWHM}(\text{neb})$ for all the sample. The meaning of the symbols and the colors is the same as in Figure 7. The solid line shows the one-to-one relation between the two FWHMs, while the dotted line is a relation between the two after taking into account an additional scattering of $\text{Ly}\alpha$ photons by residual H_I atoms in the H_II region, $\text{FWHM}_{\text{int}}(\text{Ly}\alpha) = \text{FWHM}(\text{neb}) + 200$.

duced not only from recombination of hydrogen gas ionized in HII regions, but also from e.g., shock heating (Otí-Flóranes et al. 2012), fluorescence (e.g., Cantalupo et al. 2012, 2014), and/or gravitational cooling (e.g., Dijkstra et al. 2006). If these are taken into account, the huge $\text{FWHM}_{\text{int}}(\text{Ly}\alpha)$ in the blue bump objects could be explained as follows.

Fluorescence caused by a QSO would ionize the outer layer of the ISM of galaxies, and produce a large $\text{FWHM}_{\text{int}}(\text{Ly}\alpha)$. However, there are no QSOs around any of our objects.

Gravitational cooling is another mechanism that produces $\text{Ly}\alpha$ photons. When gas inflows into the gravitational potential well of a galaxy, the gravitational binding energy is converted into the thermal energy, which is in turn released as $\text{Ly}\alpha$ photons (e.g., Dijkstra 2014). Since it occurs in both the inner and outer regions of the galaxy, gravitational cooling can give a large $\text{FWHM}_{\text{int}}(\text{Ly}\alpha)$. Furthermore, gravitational cooling can reproduce not only the observed enhanced $\text{Ly}\alpha$ blue bump flux (e.g., Dijkstra et al. 2006), but also the spatially extended $\text{Ly}\alpha$ source (Rosdahl & Blaizot 2012), i.e., diffuse $\text{Ly}\alpha$ haloes which are common features around galaxies (Steidel et al. 2011; Matsuda et al. 2012; Hayes et al. 2013; Momose et al. 2014). We note here that there exists a large uncertainty in modeling the $\text{Ly}\alpha$ emission from gravitational cooling due to its difficulty and assumed observation sensitivity (cf., Faucher-Giguère et al. 2010; Goerdt et al. 2010; Rosdahl & Blaizot 2012; Yajima et al. 2012, 2015). Our results as well as observational results quoted above can be useful for future modeling.

We conclude that not only the large discrepancy between the observed $\text{FWHM}(\text{neb})$ and $\text{FWHM}_{\text{int}}(\text{Ly}\alpha)$, but also the presence of a blue bump can be simultane-

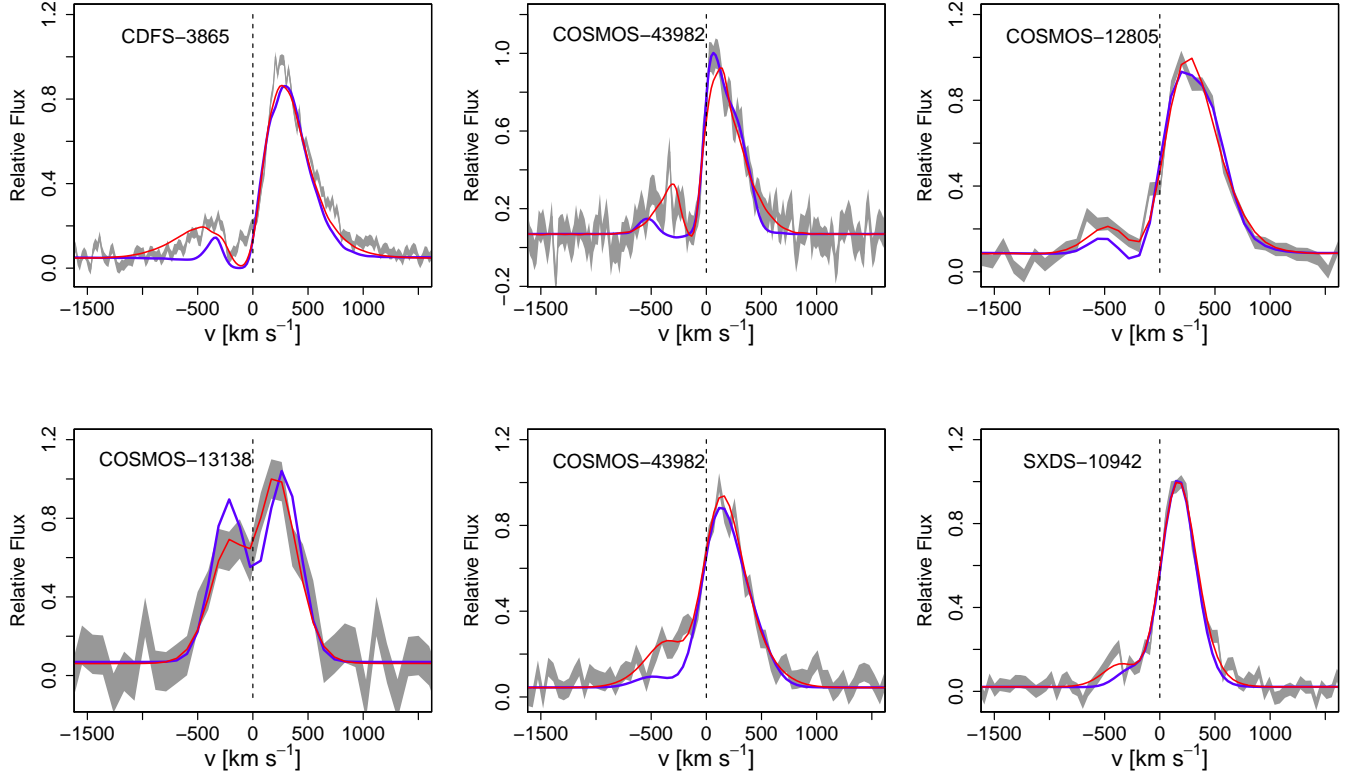


FIG. 9.— Ly α fittings with fixed $\text{FWHM}_{\text{int}}(\text{Ly}\alpha) = \text{FWHM}(\text{neb})$ for the objects with a blue bump. The reproduced Ly α lines (blue) are overlaid on the observed ones (grey). For comparison, we also plot the reproduced profiles without fixing $\text{FWHM}_{\text{int}}(\text{Ly}\alpha)$ (red).

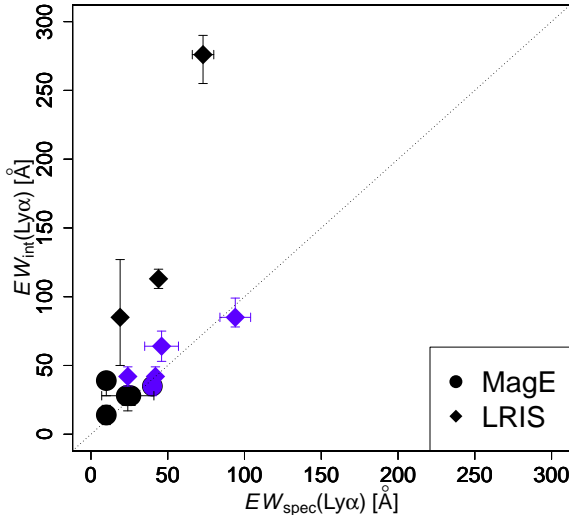


FIG. 10.— $\text{EW}_{\text{int}}(\text{Ly}\alpha)$ plotted against $\text{EW}(\text{Ly}\alpha)$ obtained from spectroscopy. The meaning of the symbols and colors is the same as in Figure 7. Since we have assumed a uniform shell model which does not cause a $\text{EW}(\text{Ly}\alpha)$ boost, the data points are expected to lie above the one-to-one relation.

ously explained if we introduce additional Ly α photons produced by gravitational cooling.

5.2. Origin of Small $\Delta v_{\text{Ly}\alpha, \text{r}}$ in LAEs

As described in §3.4, the mean $\Delta v_{\text{Ly}\alpha, \text{r}}$ of LAEs, $\simeq 200 \text{ km s}^{-1}$, is significantly smaller than that of LBGs, $\Delta v_{\text{Ly}\alpha, \text{r}} \simeq 400 \text{ km s}^{-1}$ (LBGs: e.g., Steidel et al. 2010; Rakic et al. 2011; Kulas et al. 2012; Schenker et al. 2013, LAEs: e.g., McLinden et al. 2011; Hashimoto et al. 2013; Chonis et al. 2013; Shibuya et al. 2014b; Erb et al. 2014). We have also demonstrated that some LAEs have an extremely small $\Delta v_{\text{Ly}\alpha, \text{r}}$ of $\lesssim 100 \text{ km s}^{-1}$. Hashimoto et al. (2013) and Shibuya et al. (2014b) have also found that $\Delta v_{\text{Ly}\alpha, \text{r}}$ correlates with SFR, velocity dispersion, stellar mass, specific SFR, and dust extinction. Erb et al. (2014) have also found that $\Delta v_{\text{Ly}\alpha, \text{r}}$ correlates with velocity dispersion. In addition, they find that objects with a small $\Delta v_{\text{Ly}\alpha, \text{r}}$ have a large fraction of emission blueward of the systemic velocity, while the red wing of the Ly α profile and the outflow velocity traced by absorption lines remain unchanged. Following these findings, Erb et al. (2014) have argued that the small $\Delta v_{\text{Ly}\alpha, \text{r}}$ in LAEs is consistent with a scenario where the opacity to Ly α photons is reduced by a bulk motion and/or covering fraction of the gas near the systemic velocity (see also Steidel et al. 2010). These results suggest that $\Delta v_{\text{Ly}\alpha, \text{r}}$ is closely related with the physical size of the galaxy system. However, there are still no definitive conclusions why LAEs have small $\Delta v_{\text{Ly}\alpha, \text{r}}$.

In this subsection, we explore the origin of the small $\Delta v_{\text{Ly}\alpha, \text{r}}$ in LAEs using the largest sample of LAEs whose high-quality spectroscopy data and several properties have been obtained. There are several hypotheses which give $\Delta v_{\text{Ly}\alpha, \text{r}}$ as small as $0 - 200 \text{ km}$

s^{-1} : a uniform shell ISM with a high-speed galactic outflow (e.g., Verhamme et al. 2006), a uniform shell ISM with a low neutral hydrogen column density (e.g., Verhamme et al. 2006, 2015), and other models such as a clumpy ISM with a low covering factor f_c (Hansen & Oh 2006; Dijkstra & Kramer 2012; Laursen et al. 2013), or shell models with holes/cavities, i.e., $CF < 1$ (e.g., Behrens et al. 2014; Verhamme et al. 2015). We quantitatively discuss the first two hypotheses based on our detailed comparison of data with uniform shell models (§5.2.1 and §5.2.2), then qualitatively discuss other models (§5.2.3).

5.2.1. High Outflow Velocity

An outflow velocity larger than $V_{\text{exp}} \sim 300 \text{ km s}^{-1}$ can reduce $\Delta v_{\text{Ly}\alpha, r}$ because Ly α photons would drop out of resonance with H I atoms in the outflowing gas (e.g., Verhamme et al. 2006, 2015). However, our results of Ly α radiative transfer fitting in §4.3.2 show that all objects have small V_{exp} of $100 - 200 \text{ km s}^{-1}$. Combined with the findings in §4.5.1 that these V_{exp} are consistent with the observed outflow velocities, Δv_{abs} , we conclude that the high outflow velocity hypothesis is unlikely.

5.2.2. Low N_{HI}

We examine the low N_{HI} hypothesis. Although it is difficult to directly measure N_{HI} in LAEs from observations, we have inferred it using the expanding shell model (§4.3.2). If we exclude the blue-bump objects from the sample, modeled Ly α profiles and parameters are all consistent with the observed Ly α profiles and several fundamental observables. Thus, we consider the derived neutral hydrogen column density, N_{HI} , to be reliable as well. Figure 11 is a plot of $\Delta v_{\text{Ly}\alpha, r}$ against $\log(N_{\text{HI}})$ for the non-blue bump objects. We add results from the literature: Verhamme et al. (2008), Schaerer & Verhamme (2008), Vanzella et al. (2010), and Dessauges-Zavadsky et al. (2010). These authors have also utilized the model used in this study for $z \sim 3$ LBGs with various EW(Ly α) (Verhamme et al. 2008), a strongly lensed LBG with Ly α absorption at $z \sim 2.73$ (MS 1512-cB58) (Schaerer & Verhamme 2008), a peculiar $z = 5.56$ [NIV emitter with EW(Ly α) = 89 Å (Vanzella et al. 2010), and a lensed LBG with Ly α absorption, “the 8 o’clock arc” (Dessauges-Zavadsky et al. 2010). We also add the results of Kulas et al. (2012) and Chonis et al. (2013), although models used in these studies are different from the one used in this study. In the figure, objects with EW(Ly α) $\gtrsim 30 \text{ Å}$ are colored in red and labeled as LAEs, while those with EW(Ly α) $< 30 \text{ Å}$ are colored in blue and labeled as LBGs.

We caution readers that all the data points and error bars in Figure 11 are obtained assuming uniform expanding shell models (see §4.2 for how we have obtained the error bars of our data points). The results can be significantly changed once if we consider other theoretical models such as clumpy or patchy models (see §5.2.3).

The figure shows a clear correlation between $\log(N_{\text{HI}})$ and $\Delta v_{\text{Ly}\alpha, r}$. As described in §4.3.2, the mean $\log(N_{\text{HI}})$ in $z \sim 2$ LAEs is $\log(N_{\text{HI}}) = 18.9 \text{ cm}^{-2}$, which is more than one order of magnitude lower than those of $z \gtrsim 3$ LBGs, ~ 20.0 . We have excluded the 5 blue bump ob-

jects in our 12 LAEs in Figure 11 for a secure discussion. However, we note that they have comparable N_{HI} values to the non-blue bump objects, and are consistent with the correlation. We conclude that the small $\Delta v_{\text{Ly}\alpha, r}$ in the LAEs can be well explained by the low N_{HI} hypothesis.

5.2.3. Other Models

Throughout the paper, we have assumed a uniform expanding shell models constructed by Verhamme et al. (2006) and Schaerer et al. (2011). In this section, we qualitatively discuss alternative models such as clumpy and patchy models. Hansen & Oh (2006) have analytically investigated the Ly α radiative transfer in multi-phase media, especially, the one through dusty optically thick gas clumps. They have shown that radiative transfer strongly depends on covering factor, f_c (see also Dijkstra & Kramer 2012; Laursen et al. 2013). As can be seen from Figure 20 of Hansen & Oh (2006), asymmetric Ly α profiles with small $\Delta v_{\text{Ly}\alpha, r}$ can be reproduced by clumpy models with low f_c , i.e., a small average number of interaction for Ly α photons before escaping from the galaxy. Recently, Behrens et al. (2014) and Verhamme et al. (2015) have investigated the Ly α radiative transfer in a shell with holes and/or cavities, i.e., $CF < 1$. These studies have shown that, if a shell has holes, the modeled Ly α line profile through a transparent line of sight has $\Delta v_{\text{Ly}\alpha, r} = 0 \text{ km s}^{-1}$ even if convolved with spectral resolutions used for the observations (see Figures 4 and 5 in Verhamme et al. 2015). We qualitatively test the hypothesis by comparing Ly α and nebular emission line profiles. In the case of a patchy ISM, if we observe the galaxy through a transparent line of sight, observed Ly α line profiles would be indistinguishable from nebular emission line profiles. This is because the main Ly α component is dominant and is not affected by the radiative transfer effect. As can be seen in Figure 1, COSMOS-08357 and COSMOS-43982 have indistinguishable Ly α and nebular line profiles. We conclude that at least two objects, COSMOS-08357 and COSMOS-43982, could be explained by patchy ISM models.

Thus, we have demonstrated that the small $\Delta v_{\text{Ly}\alpha, r}$ in LAEs can be also well reproduced by clumpy and/or patchy ISM. However, future detailed Ly α modeling assuming clumpy and patchy ISM are needed for a more definitive conclusion. Whichever hypothesis is the most relevant one, the key for the small $\Delta v_{\text{Ly}\alpha, r}$ in LAEs would be the reduced number of resonant scattering of Ly α photons.

Hereafter in this section, we focus on the results obtained from uniform expanding shell models with low N_{HI} .

5.3. Interpretation of Low N_{HI} in LAEs

We have shown that, on the assumption of uniform shell models, the most likely situation for the smaller $\Delta v_{\text{Ly}\alpha, r}$ in the present sample is that LAEs have low N_{HI} . We can envisage three possible scenarios for LAEs having low N_{HI} .

First, it is possible that LAEs have a low H I gas mass. Indeed, Pardy et al. (2014) have detected an H I 21cm line for 14 local galaxies with Ly α emission (Lyman Alpha Reference Sample; Östlin et al. 2014), to find that

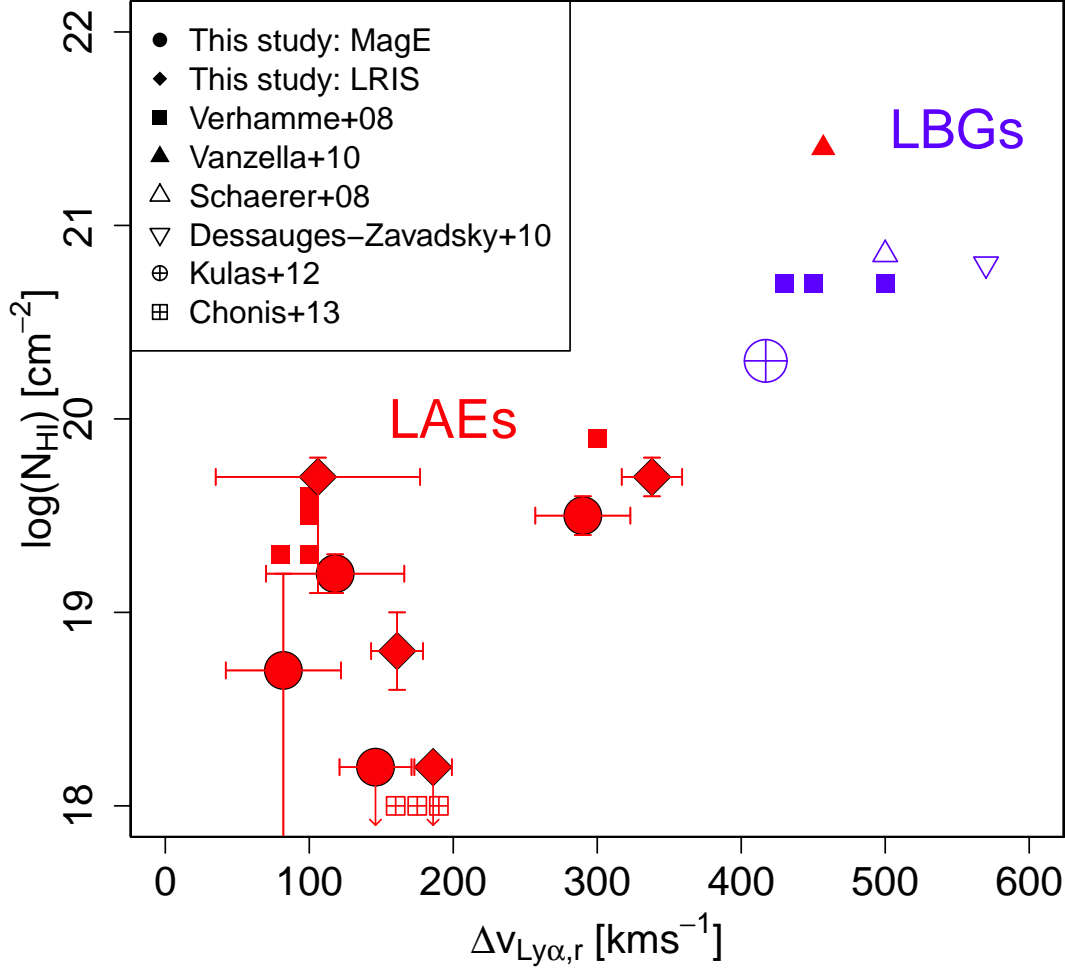


FIG. 11.— $\log(N_{\text{HI}})$ plotted against $\Delta v_{\text{Ly}\alpha, \text{r}}$. Red (blue) symbols correspond to objects with $\text{EW}(\text{Ly}\alpha)_{\text{photo}}$ larger (smaller) than 30 \AA . Filled circles and diamonds are the non blue bump LAEs obtained by MagE and LIRS, respectively. Filled squares show $z \sim 3$ objects given by Verhamme et al. (2008). A filled triangle denotes a $z = 5.56$ [NIV emitter with $\text{EW}(\text{Ly}\alpha) = 89 \text{ \AA}$] (Vanzella et al. 2010). An open triangle is a lensed LBG with Ly α absorption, cB58 (Schaerer & Verhamme 2008), while an inverted triangle is a lensed LBG with Ly α absorption, “the 8 o’clock arc” (Dessauges-Zavadsky et al. 2010). In addition, the objects studied in Kulas et al. (2012) and Chonis et al. (2013) are plotted as a circle and three squares with a cross inside, respectively. For the purpose of display, three LAEs given by Chonis et al. (2013) which have similar $\Delta v_{\text{Ly}\alpha, \text{r}}$ and $\log(N_{\text{HI}})$ values of 175 km s^{-1} and 18 cm^{-2} , are shifted toward x-axis. We stress that all the data points and error bars are obtained assuming uniform expanding shells. The positions and/or error bars of data points in the figure can be significantly changed if we consider other models. See the text (§5.2.2) for the detail.

the derived HI gas mass tentatively anti-correlates with $\text{EW}(\text{Ly}\alpha)$. This trend is also consistent with theoretical predictions (private communications with T. Garel and C. Lagos).

Second, if a galaxy has a high gas ionization state, ionizing photons would efficiently ionize the neutral gas in the ISM. This would decrease the thickness of the HI gas in the outflowing shell, and lower their N_{HI} . This picture is consistent with the recent finding of Nakajima & Ouchi (2014) that LAEs have a significantly higher ionization state than that of LBGs at the same redshift. The high ionization state in LAEs would be due to their young stellar populations (e.g., Pirzkal et al. 2007; Ono et al. 2010b,a). Young O- and B type stars in LAEs would efficiently produce ionizing photons, and re-

duce the N_{HI} of the surrounding gas.

Finally, in the case of a face-on galaxy, we would see a lower N_{HI} because Ly α photons would experience a shorter path length out of the disk (e.g., Verhamme et al. 2012; Zheng & Wallace 2014). Indeed, Shibuya et al. (2014a) have statistically examined the ellipticity, an indicator of the inclination, for $z \sim 2$ LAEs using *HST* data. A weak trend has been found that high $\text{EW}(\text{Ly}\alpha)$ objects are less inclined.

A combination of these effects would reduce the number of resonant scatterings of Ly α photons. This would, in turn, decrease the Ly α velocity offset, $\Delta v_{\text{Ly}\alpha, \text{r}}$ (e.g., McLinden et al. 2011; Hashimoto et al. 2013; Erb et al. 2014) and the Ly α spatial offset, $\delta_{\text{Ly}\alpha}$ (Jiang et al. 2013; Shibuya et al. 2014a).

5.4. Implication of Small $\Delta v_{\text{Ly}\alpha, \text{r}}$ and Δv_{peak} in LAEs

Recent theoretical studies (Behrens et al. 2014; Verhamme et al. 2015) have proposed that the Ly α line profile can be used as a probe of Lyman continuum (LyC; $\lambda < 912\text{\AA}$) leaking galaxies (LyC leakers). LyC leakers are thought to have contributed to cosmic reionization. Observationally, detections of LyC emission are claimed for LAEs and LBGs both spectroscopically (e.g., Shapley et al. 2006) and photometrically (e.g., Iwata et al. 2009 and Nestor et al. 2013). However, the success rate is very low possibly because LyC leakers are extremely faint objects (e.g., Ouchi et al. 2008).

Verhamme et al. (2015) have investigated two scenarios for the ionizing photon escape: (1) the density bounded HII regions with an extremely low N_{HI} value, $\log(N_{\text{HI}}) \lesssim 17.0 \text{ cm}^{-2}$, corresponding to an unity optical depth for ionizing photons, (2) or a galaxy has a partial spatial covering fraction of the gas. They have shown that $\Delta v_{\text{Ly}\alpha, \text{r}}$ (Δv_{peak} , if the blue bump exists) is extremely small in these cases, $\Delta v_{\text{Ly}\alpha, \text{r}} \lesssim 100 \text{ km s}^{-1}$ ($\Delta v_{\text{peak}} \lesssim 150 \text{ km s}^{-1}$) (see also Jaskot & Oey 2014; Martin et al. 2015).

On the other hand, as described in §3.4, objects with a large EW(Ly α) value tend to have a small $\Delta v_{\text{Ly}\alpha, \text{r}}$ (Δv_{peak}), implying that they are good candidates of LyC leakers. If the ionizing photon escape fraction, f_{esc} , is high, the recombination Ly α line might be weakened. However, as Nakajima & Ouchi (2014) have shown, EW(Ly α) can be as high as 100 \AA even at $f_{\text{esc}} \sim 0.5$.

Thus, we propose that selecting objects with EW(Ly α) as large as 100\AA is a promising way to search for LyC leaking galaxies. The merit of this candidate selection technique is that it does not require spectroscopy.

6. SUMMARY AND CONCLUSION

We have presented the results of a Ly α profile analysis of twelve LAEs at $z \sim 2.2$ for which high spectral resolution Ly α lines are obtained in Hashimoto et al. (2013) and Shibuya et al. (2014b) with Magellan/MagE or Keck/LRIS. Two objects have been observed with both spectrographs. All twelve objects have detections of nebula emission lines which are used not only to define the systemic redshift but also to infer the intrinsic FWHM of the Ly α line. We have also derived the galactic outflow velocity from blueshifted low-ionization state (LIS) metal absorption lines with respect to the systemic redshift for three individual LRIS spectra as well as for a stacked spectrum of four MagE spectra. In addition, we have obtained stellar dust extinction from SED fit. The high spectral resolution Ly α data in conjunction with these measurements have enabled us to perform detailed comparisons between observed and modeled Ly α lines. Our main results are as follows.

- We find that all 12 objects have Ly α profiles with a main peak redward of the systemic redshift and five objects (six spectra) have a weak, secondary peak blueward of the systemic redshift (the blue bump). For a sample of 17 objects from our study and the literature with a resolved Ly α line, we estimate the ratio of LAEs with a blue bump to be $\sim 50\%$, which is slightly higher than that of

LBGs. We have obtained $\Delta v_{\text{Ly}\alpha, \text{r}} = 174 \pm 19 \text{ km s}^{-1}$ ($\Delta v_{\text{Ly}\alpha, \text{b}} = -316 \pm 45 \text{ km s}^{-1}$), which is smaller than (comparable to) that of LBGs, $\Delta v_{\text{Ly}\alpha, \text{r}} \simeq 400 \text{ km s}^{-1}$ ($\Delta v_{\text{Ly}\alpha, \text{b}} = -367 \pm 46 \text{ km s}^{-1}$).

- The high spectral resolution and sensitivity of Subaru/FMOS have enabled us to detect two-component [OIII] profiles in two LAEs for the first time. While its origin is not clear, we find that even the FWHM of the broad component is as small as $70 - 80 \text{ km s}^{-1}$. This excludes the possibility of its origin being AGN activity or powerful hot outflows.
- We have applied the uniform expanding shell model constructed by Verhamme et al. (2006) and Schaerer et al. (2011) to our sample. The model successfully reproduces not only Ly α profiles but also the galactic outflow velocity measured from LIS absorption lines and the FWHM of nebular emission lines for the non blue-bump objects. However, for the blue-bump objects, the intrinsic FWHMs of Ly α predicted by the model is significantly larger than the observed FWHMs of nebular emission lines.
- For the blue bump objects, we have tried another fit fixing the intrinsic FWHM of Ly α to the observed FWHM of nebular emission lines. The position and flux of the blue bump are poorly reproduced.
- To understand the large discrepancy between FWHM_{int}(Ly α) and FWHM(neb) in the blue-bump objects, we have examined if objects with and without a blue bump have different properties such as the Ly α luminosity, stellar mass, and the merger fraction. We find no significant difference between the two samples. We propose that taking into account Ly α photons produced by gravitational cooling might simultaneously explain the large FWHM_{int}(Ly α) and the existence of a blue bump.
- We quantitatively demonstrate that the small $\Delta v_{\text{Ly}\alpha, \text{r}}$ in LAEs can be well explained by uniform expanding shell models with neutral hydrogen column density as low as $\log(N_{\text{HI}}) = 18.9 \text{ cm}^{-2}$. This value is more than one order of magnitude lower than that of LBGs, and is consistent with the recent findings that LAEs have a high ionization parameter and a low HI gas mass. These results imply that low N_{HI} is the key for the small $\Delta v_{\text{Ly}\alpha, \text{r}}$ as well as the Ly α escape mechanism. However, we caution readers that our results are based only on uniform expanding shell models, and that future detailed modeling with clumpy and/or patchy ISM are needed for a definitive conclusion.
- As an implication of the small $\Delta v_{\text{Ly}\alpha, \text{r}}$ and low N_{HI} in high EW(Ly α) objects, we propose that targeting high EW(Ly α) objects would be an efficient way to search for Lyman Continuum leaking galaxies from photometry data alone.

ACKNOWLEDGEMENTS

We thank an anonymous referee for valuable comments that have greatly improved the paper. We are grateful to Thibault Garel, Claudia Lagos, Ivana Orlitová, Kentaro Motohara, Nobunari Kashikawa, Ryohei Kawabe, Koharo Kohno, and Toru Yamada for their helpful comments and suggestions. We acknowledge Richard Ellis and Matthew Schenker for kindly providing us with their LBG data. We also thank George Becker for making the

software package **MagE_REDUCE** available to us. This work was supported by World Premier International Research Center Initiative (WPI Initiative), MEXT, Japan, and KAKENHI (23244022) and (23244025) Grant-in-Aid for Scientific Research (A) through Japan Society for the Promotion of Science (JSPS). T.H. also acknowledges the JSPS Research Fellowship for Young Scientists. A.V. was supported by a Fellowship “Boursière d’Excellence” of Geneva University. M.R. was supported by a grant AST-1108815 from the National Science Foundation.

APPENDIX

Figures 12 - 14 show 2D χ^2 contours for CDFS-3865. All the grids are shown in grey dots. The blue (red) grids in these figures show those satisfying $\Delta\chi^2 \leq 6.17$ (11.8) above the raw minimum χ^2 designated by the white dots, i.e., the 3 (5) σ uncertainty in the parameters (Press et al. 1992).

REFERENCES

- Abraham, R. G., van den Bergh, S., Glazebrook, K., Ellis, R. S., Santiago, B. X., Surma, P., & Griffiths, R. E. 1996, *ApJS*, 107, 1
- Atek, H., Kunth, D., Schaerer, D., Mas-Hesse, J. M., Hayes, M., Östlin, G., & Kneib, J.-P. 2014, *A&A*, 561, A89
- Baldwin, J. A., Phillips, M. M., & Terlevich, R. 1981, *PASP*, 93, 5
- Behrens, C., & Braun, H. 2014, *A&A*, 572, A74
- Behrens, C., Dijkstra, M., & Niemeyer, J. C. 2014, *A&A*, 563, A77
- Bond, N. A., Gawiser, E., Gronwall, C., Ciardullo, R., Altmann, M., & Schawinski, K. 2009, *ApJ*, 705, 639
- Calzetti, D., Armus, L., Bohlin, R. C., Kinney, A. L., Koornneef, J., & Storchi-Bergmann, T. 2000, *ApJ*, 533, 682
- Cantalupo, S., Arrigoni-Battaia, F., Prochaska, J. X., Hennawi, J. F., & Madau, P. 2014, *Nature*, 506, 63
- Cantalupo, S., Lilly, S. J., & Haehnelt, M. G. 2012, *MNRAS*, 425, 1992
- Cardamone, C., et al. 2009, *MNRAS*, 399, 1191
- Cassata, P., et al. 2015, *A&A*, 573, A24
- Chonis, T. S., et al. 2013, *ApJ*, 775, 99
- Christensen, L., et al. 2012, *MNRAS*, 427, 1973
- Conselice, C. J., Bershadsky, M. A., & Jangren, A. 2000, *ApJ*, 529, 886
- Cooke, J., Berrier, J. C., Barton, E. J., Bullock, J. S., & Wolfe, A. M. 2010, *MNRAS*, 403, 1020
- Cowie, L. L., Barger, A. J., & Hu, E. M. 2011, *ApJ*, 738, 136
- Deharveng, J.-M., et al. 2008, *ApJ*, 680, 1072
- Dessauges-Zavadsky, M., D’Odorico, S., Schaerer, D., Modigliani, A., Tapken, C., & Vernet, J. 2010, *A&A*, 510, A26
- Dijkstra, M. 2014, *ArXiv e-prints*
- Dijkstra, M., Haiman, Z., & Spaans, M. 2006, *ApJ*, 649, 14
- Dijkstra, M., & Kramer, R. 2012, *MNRAS*, 424, 1672
- Dijkstra, M., & Loeb, A. 2009, *MNRAS*, 396, 377
- Duval, F., Schaerer, D., Östlin, G., & Laursen, P. 2014, *A&A*, 562, A52
- Erb, D. K., Pettini, M., Shapley, A. E., Steidel, C. C., Law, D. R., & Reddy, N. A. 2010, *ApJ*, 719, 1168
- Erb, D. K., Shapley, A. E., Pettini, M., Steidel, C. C., Reddy, N. A., & Adelberger, K. L. 2006a, *ApJ*, 644, 813
- Erb, D. K., Steidel, C. C., Shapley, A. E., Pettini, M., Reddy, N. A., & Adelberger, K. L. 2006b, *ApJ*, 646, 107
- Erb, D. K., et al. 2014, *ArXiv e-prints*
- Faucher-Giguère, C.-A., Kereš, D., Dijkstra, M., Hernquist, L., & Zaldarriaga, M. 2010, *ApJ*, 725, 633
- Finkelstein, S. L., et al. 2011, *ApJ*, 729, 140
- Gawiser, E., et al. 2007, *ApJ*, 671, 278
- Genzel, R., et al. 2011, *ApJ*, 733, 101
- Goedert, T., Dekel, A., Sternberg, A., Ceverino, D., Teyssier, R., & Primack, J. R. 2010, *MNRAS*, 407, 613
- Gronke, M., & Dijkstra, M. 2014, *MNRAS*, 444, 1095
- Guaita, L., Francke, H., Gawiser, E., Bauer, F. E., Hayes, M., Östlin, G., & Padilla, N. 2013, *A&A*, 551, A93
- Guaita, L., et al. 2010, *ApJ*, 714, 255
- . 2011, *ApJ*, 733, 114
- Hagen, A., et al. 2014, *ApJ*, 786, 59
- Hansen, M., & Oh, S. P. 2006, *MNRAS*, 367, 979
- Harikane, Y., Ouchi, M., Yuma, S., Rauch, M., Nakajima, K., & Ono, Y. 2014, *ArXiv e-prints*
- Hashimoto, T., Ouchi, M., Shimasaku, K., Ono, Y., Nakajima, K., Rauch, M., Lee, J., & Okamura, S. 2013, *ApJ*, 765, 70
- Hayes, M., et al. 2013, *ApJ*, 765, L27
- Heckman, T. M., et al. 2011, *ApJ*, 730, 5
- Henry, A., Scarlata, C., Martin, C. L., & Erb, D. 2015, *ArXiv e-prints*
- Hu, E. M., & McMahon, R. G. 1996, *Nature*, 382, 231
- Iwata, I., et al. 2009, *ApJ*, 692, 1287
- Jaskot, A. E., & Oey, M. S. 2014, *ApJ*, 791, L19
- Jiang, L., et al. 2013, *ApJ*, 773, 153
- Kashino, D., et al. 2013, *ApJ*, 777, L8
- Kelson, D. D. 2003, *PASP*, 115, 688
- Kollmeier, J. A., Zheng, Z., Davé, R., Gould, A., Katz, N., Miralda-Escudé, J., & Weinberg, D. H. 2010, *ApJ*, 708, 1048
- Kornei, K. A., Shapley, A. E., Erb, D. K., Steidel, C. C., Reddy, N. A., Pettini, M., & Bogosavljević, M. 2010, *ApJ*, 711, 693
- Kulas, K. R., Shapley, A. E., Kollmeier, J. A., Zheng, Z., Steidel, C. C., & Hainline, K. N. 2012, *ApJ*, 745, 33
- Kunth, D., Mas-Hesse, J. M., Terlevich, E., Terlevich, R., Lequeux, J., & Fall, S. M. 1998, *A&A*, 334, 11
- Kusakabe, H., Shimasaku, K., Nakajima, K., & Ouchi, M. 2015, *ApJ*, 800, L29
- Laursen, P., Duval, F., & Östlin, G. 2013, *ApJ*, 766, 124
- Law, D. R., Steidel, C. C., Shapley, A. E., Nagy, S. R., Reddy, N. A., & Erb, D. K. 2012, *ApJ*, 745, 85
- Le Fèvre, O., et al. 2000, *MNRAS*, 311, 565
- Lidman, C., Hayes, M., Jones, D. H., Schaerer, D., Westra, E., Tapken, C., Meisenheimer, K., & Verhamme, A. 2012, *MNRAS*, 420, 1946
- Malhotra, S., Rhoads, J. E., Finkelstein, S. L., Hathi, N., Nilsson, K., McLinden, E., & Pirzkal, N. 2012, *ApJ*, 750, L36
- Martin, C. L. 2005, *ApJ*, 621, 227
- Martin, C. L., Dijkstra, M., Henry, A., Soto, K. T., Danforth, C. W., & Wong, J. 2015, *ApJ*, 803, 6
- Matsuda, Y., et al. 2012, *MNRAS*, 425, 878
- McLinden, E. M., et al. 2011, *ApJ*, 730, 136
- Momose, R., et al. 2014, *MNRAS*, 442, 110
- Mosleh, M., et al. 2012, *ApJ*, 756, L12
- Nakajima, K., & Ouchi, M. 2014, *MNRAS*, 442, 900
- Nakajima, K., Ouchi, M., Shimasaku, K., Hashimoto, T., Ono, Y., & Lee, J. C. 2013, *ArXiv e-prints*
- Nakajima, K., et al. 2012, *ApJ*, 745, 12
- Nestor, D. B., Shapley, A. E., Kornei, K. A., Steidel, C. C., & Siana, B. 2013, *ApJ*, 765, 47
- Neufeld, D. A. 1991, *ApJ*, 370, L85
- Newman, S. F., et al. 2012, *ApJ*, 761, 43
- Nilsson, K. K., et al. 2007, *A&A*, 471, 71
- Oke, J. B., & Gunn, J. E. 1983, *ApJ*, 266, 713
- Ono, Y., Ouchi, M., Shimasaku, K., Dunlop, J., Farrah, D., McLure, R., & Okamura, S. 2010a, *ApJ*, 724, 1524
- Ono, Y., et al. 2010b, *MNRAS*, 402, 1580

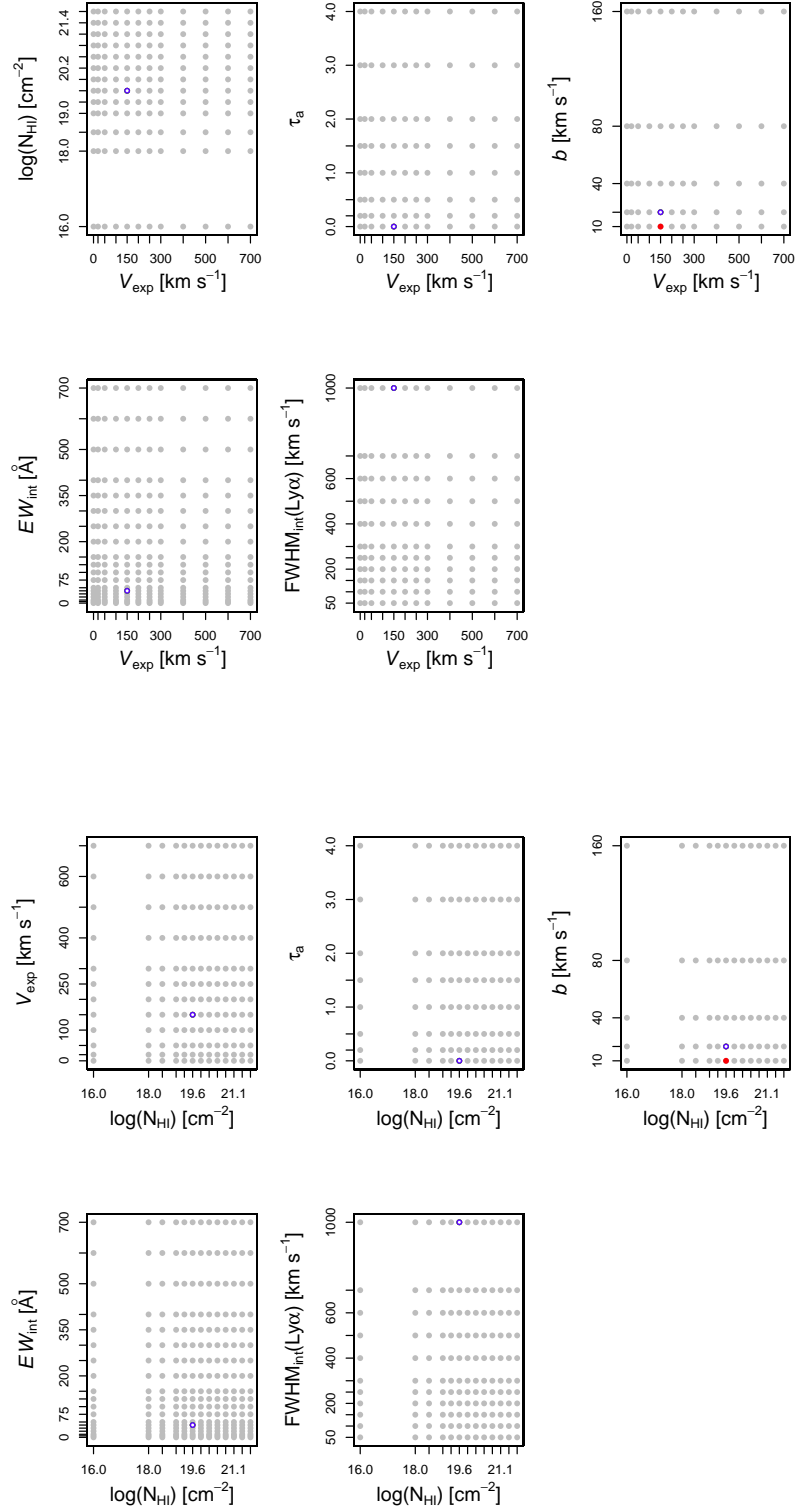


FIG. 12.— Upper and lower five panels show 2D χ^2 contours for V_{exp} and $\log(N_{\text{HI}})$, respectively, for CDFS-3865. The grids colored with blue (red) denote those within the 3 (5) σ level from the minimum χ^2 grid shown as a white dot.

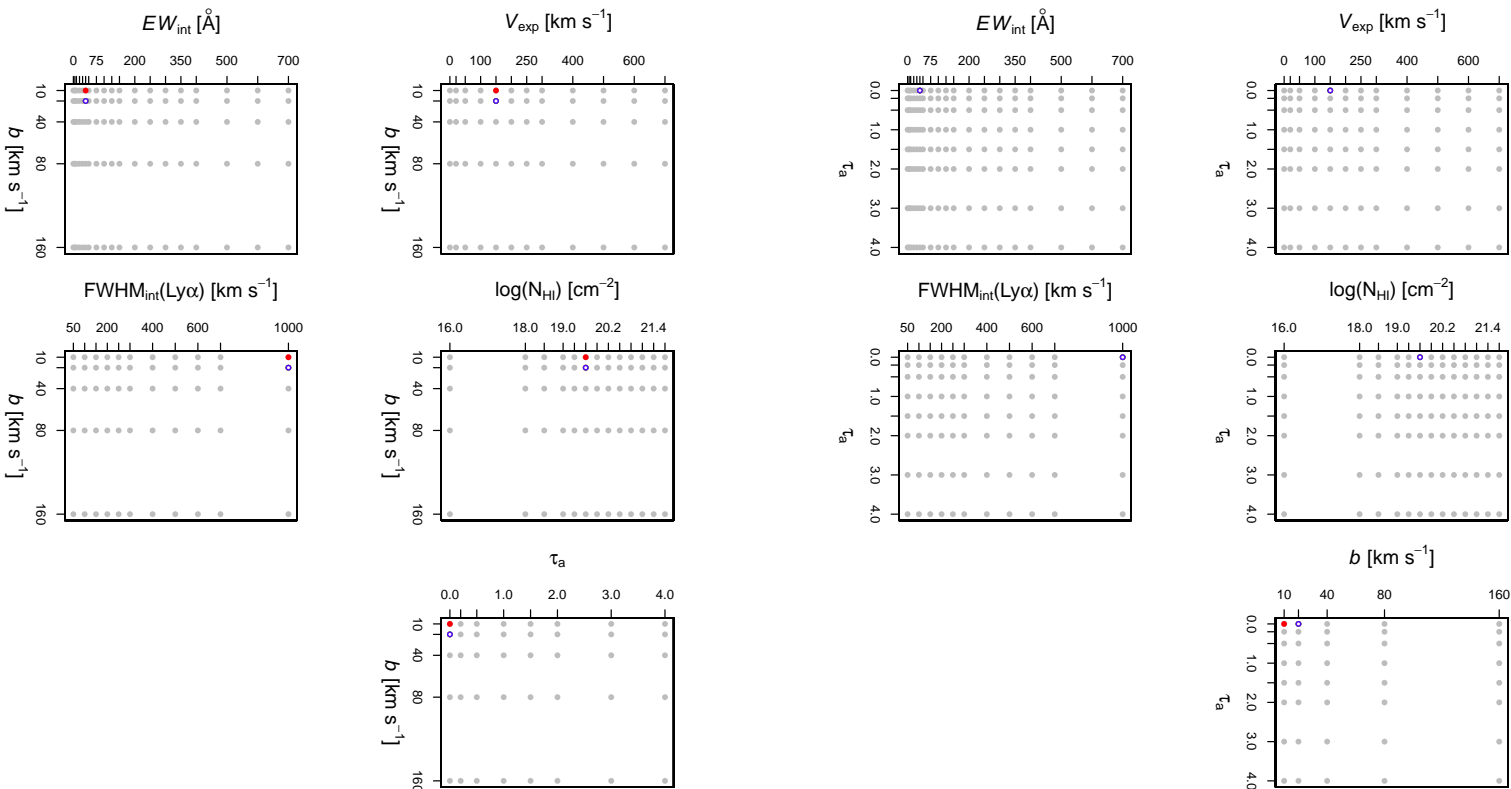


FIG. 13.— Upper and lower five panels show 2D χ^2 contours for τ_a and b , respectively, for CDFS-3865. The meaning of the colors is the same as in Figure 12.

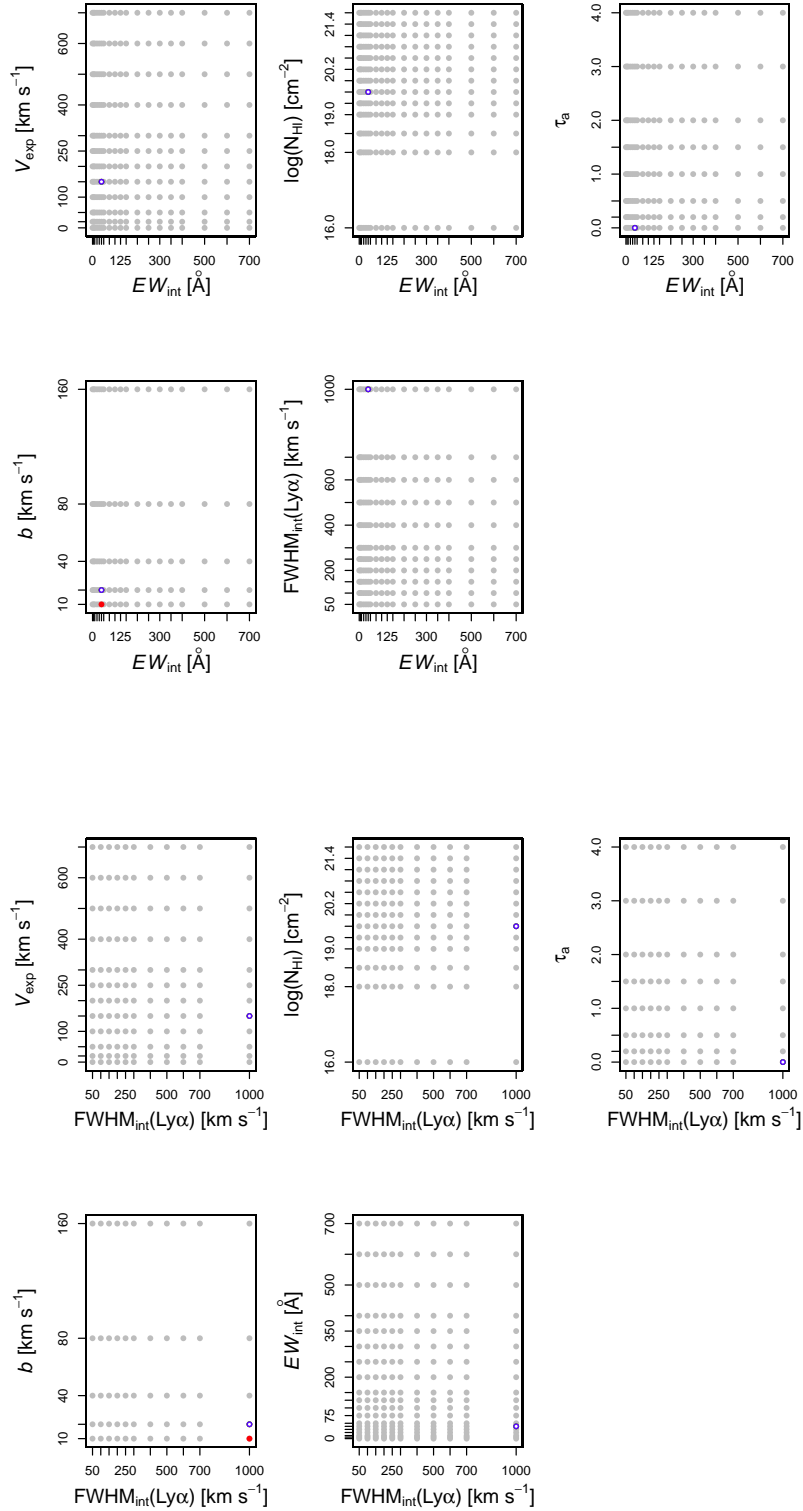


FIG. 14.— Upper and lower five panels show 2D χ^2 contours for $EW_{\text{int}}(\text{Ly}\alpha)$ and $\text{FWHM}_{\text{int}}(\text{Ly}\alpha)$, respectively, for CDFS-3865. The meaning of the colors is the same as in Figure 12.

- . 2013, *ApJ*, 777, 155
- Osterbrock, D. E., & Ferland, G. J. 2006, *Astrophysics of gaseous nebulae and active galactic nuclei*
- Östlin, G., et al. 2014, *ApJ*, 797, 11
- Oti-Floranes, H., Mas-Hesse, J. M., Jiménez-Bailón, E., Schaerer, D., Hayes, M., Östlin, G., Atek, H., & Kunth, D. 2012, *A&A*, 546, A65
- Ouchi, M., et al. 2008, *ApJS*, 176, 301
- . 2010, *ApJ*, 723, 869
- Pardy, S. A., et al. 2014, *ArXiv e-prints*
- Peng, C. Y., Ho, L. C., Impey, C. D., & Rix, H.-W. 2002, *AJ*, 124, 266
- Pettini, M., Shapley, A. E., Steidel, C. C., Cuby, J.-G., Dickinson, M., Moorwood, A. F. M., Adelberger, K. L., & Giavalisco, M. 2001, *ApJ*, 554, 981
- Pirzkal, N., Malhotra, S., Rhoads, J. E., & Xu, C. 2007, *ApJ*, 667, 49
- Press, W. H., Teukolsky, S. A., Vetterling, W. T., & Flannery, B. P. 1992, *Numerical recipes in C. The art of scientific computing*
- Rakic, O., Schaye, J., Steidel, C. C., & Rudie, G. C. 2011, *MNRAS*, 414, 3265
- Rauch, M., Becker, G. D., Haehnelt, M. G., Gauthier, J.-R., Ravindranath, S., & Sargent, W. L. W. 2011, *MNRAS*, 418, 1115
- Rauch, M., et al. 2008, *ApJ*, 681, 856
- Rhoads, J. E., & Malhotra, S. 2001, *ApJ*, 563, L5
- Rosdahl, J., & Blaizot, J. 2012, *MNRAS*, 423, 344
- Schaerer, D., Hayes, M., Verhamme, A., & Teyssier, R. 2011, *A&A*, 531, A12
- Schaerer, D., & Verhamme, A. 2008, *A&A*, 480, 369
- Schenker, M. A., Ellis, R. S., Konidaris, N. P., & Stark, D. P. 2013, *ApJ*, 777, 67
- Seaton, M. J. 1979, *MNRAS*, 187, 73P
- Shapiro, K. L., et al. 2009, *ApJ*, 701, 955
- Shapley, A. E., Steidel, C. C., Pettini, M., & Adelberger, K. L. 2003, *ApJ*, 588, 65
- Shapley, A. E., Steidel, C. C., Pettini, M., Adelberger, K. L., & Erb, D. K. 2006, *ApJ*, 651, 688
- Shibuya, T., Ouchi, M., Nakajima, K., Yuma, S., Hashimoto, T., Shimasaku, K., Mori, M., & Umemura, M. 2014a, *ApJ*, 785, 64
- Shibuya, T., et al. 2014b, *ApJ*, 788, 74
- Song, M., et al. 2014, *ApJ*, 791, 3
- Soto, K. T., Martin, C. L., Prescott, M. K. M., & Armus, L. 2012, *ApJ*, 757, 86
- Steidel, C. C., Bogosavljević, M., Shapley, A. E., Kollmeier, J. A., Reddy, N. A., Erb, D. K., & Pettini, M. 2011, *ApJ*, 736, 160
- Steidel, C. C., Erb, D. K., Shapley, A. E., Pettini, M., Reddy, N., Bogosavljević, M., Rudie, G. C., & Rakic, O. 2010, *ApJ*, 717, 289
- Vanzella, E., et al. 2010, *A&A*, 513, A20
- Verhamme, A., Dubois, Y., Blaizot, J., Garel, T., Bacon, R., Devriendt, J., Guiderdoni, B., & Slyz, A. 2012, *A&A*, 546, A111
- Verhamme, A., Orlitová, I., Schaerer, D., & Hayes, M. 2015, *A&A*, 578, A7
- Verhamme, A., Schaerer, D., Atek, H., & Tapken, C. 2008, *A&A*, 491, 89
- Verhamme, A., Schaerer, D., & Maselli, A. 2006, *A&A*, 460, 397
- Yajima, H., Li, Y., Zhu, Q., & Abel, T. 2015, *ApJ*, 801, 52
- Yajima, H., Li, Y., Zhu, Q., Abel, T., Gronwall, C., & Ciardullo, R. 2012, *ApJ*, 754, 118
- Yamada, T., Matsuda, Y., Kousai, K., Hayashino, T., Morimoto, N., & Umemura, M. 2012, *ApJ*, 751, 29
- Yang, H., Malhotra, S., Gronke, M., Rhoads, J. E., Jaskot, A., Zheng, Z., & Dijkstra, M. 2015, *ArXiv e-prints*
- Yang, Y., Zabludoff, A., Jahnke, K., & Davé, R. 2014, *ApJ*, 793, 114
- Zheng, Z., & Miralda-Escudé, J. 2002, *ApJ*, 578, 33
- Zheng, Z., & Wallace, J. 2014, *ApJ*, 794, 116